Liquid Crystals
Publication details, including instructions for authors and subscription information:
http://www.informaworld.com/smpp/title~content=t713926090

Twisted smectics as the liquid crystal analogues of type II superconductors

Laurence Navailles[a]; Philippe Barois[a]
[a] Université de Bordeaux, CNRS, Centre de Recherche Paul Pascal, PESSAC, France

First published on: 12 August 2009

To cite this Article Navailles, Laurence and Barois, Philippe(2009) 'Twisted smectics as the liquid crystal analogues of type II superconductors', Liquid Crystals, 36: 10, 1241 — 1261, First published on: 12 August 2009 (iFirst)
To link to this Article: DOI: 10.1080/02678290903059271
URL: http://dx.doi.org/10.1080/02678290903059271

Liquid Crystals,
Vol. 36, Nos. 10–11, October–November 2009, 1241–1261

Taylor & Francis
Taylor & Francis Group

INVITED ARTICLE

Twisted smectics as the liquid crystal analogues of type II superconductors

Laurence Navailles and Philippe Barois*

Université de Bordeaux, CNRS, Centre de Recherche Paul Pascal, 115 Avenue Albert Schweitzer, 33600 PESSAC, France

(Received 11 May 2009; final form 20 May 2009)

In 1972, de Gennes pointed out the formal analogy between the Landau–Ginzburg Hamiltonians describing the phase transition from normal to superconductor on one hand and from nematic to smectic A liquid crystals on the other hand. This elegant analogy became a source of inspiration not only for theoreticians, as it revealed and emphasised the beauty and the richness of the physics of liquid crystals, but also for chemists in their constant search for novel liquid crystalline structures. The analogy with type I superconductors was first described and bore an appropriate educational value: the expulsion of twist in smectic liquid crystals can be viewed as equivalent to the well-known Meissner effect in superconductors. However, the investigation of the type II condition definitely opened new doors as it led to the discovery of fantastic new liquid crystal structures. In 1988, Renn and Lubensky 'invented' the Twist Grain Boundary (TGB) smectic phase as the direct analogue of the Abrikosov flux lattice. The twist penetrates the smectic layers of a TGB via a twisted lattice of screw dislocations analogous to magnetic vortices, just as the magnetic field penetrates the type II superconductor. We review in this paper the major steps of the experimental studies of the TGB phases and show that the observed behaviours closely follow the superconductor model, hence illustrating the depth of de Gennes' analogy.

Keywords: liquid crystals; chirality; phase transitions; structures; dislocations; grain boundaries; electric field effects

1. Introduction

Liquid crystals (LCs) and superconductors: what kind of similarities can be imagined between these two fields of condensed matter physics that look so different? It was the merit of de Gennes to point out in 1972 the striking – and surprising – similarity of the Landau–Ginzburg Hamiltonians that describe the phase transitions from normal to superconductor on one hand and from nematic to smectic A on the other hand (*1*). From the concepts of universality and scaling introduced by Kadanoff and Widom (see, for instance, (*2*)) in the 1960s, it followed immediately that similar physical behaviours were to be expected in the two systems. Possible illustrations of this analogy were suggested by de Gennes in his early paper (*1*), but it took 16 years and the pioneering work of Renn and Lubensky (*3*) to imagine, in 1988, the structure of the LC analogue of the Abrikosov flux phase appearing in type II superconductors. The result is the incredibly dislocated, twisted, but perfectly regular structure of the Twist Grain Boundary (TGB) smectic phase. The importance and the power of the analogy became obvious soon after with the experimental discovery of the first TGB phase by Goodby *et al.* in 1989 (*4*). The aim of this paper is to review the story of this fantastic analogy and its experimental implications, hence paying a tribute to one of the many visionary inputs of Pierre-Gilles de Gennes in the physics of LCs (*5*).

2. Liquid crystals

LCs or mesophases are intermediate states of condensed matter that combine long-range positional or orientational order along some directions of space (as in a crystal) and liquid-like disorder along other directions. The most common liquid crystalline phases can be obtained with organic molecules or in solutions of surfactants. In the first case, the phase transitions are triggered by changing the temperatures (so-called thermotropic LCs), whereas the structures are controlled by the fraction of solvent in the second case (lyotropic LCs). We will mostly restrict our attention to thermotropic LCs made of elongated (or rod-like) organic molecules, since TGBs were discovered and extensively studied in these systems, but other molecular shapes and lyotropic LCs will be addressed in Section 9.

2.1 The nematic phase

In the nematic phase (N), the mesogens exhibit no long-range positional order, as in an isotropic liquid, but instead exhibit long-range orientational order. The long axes of the molecules are preferentially

*Corresponding author: barois@crpp-bordeaux.cnrs.fr

ISSN 0267-8292 print/ISSN 1366-5855 online

DOI: 10.1080/02678290903059271
http://www.informaworld.com

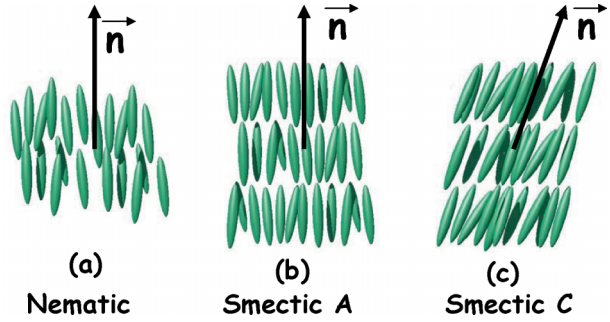

Figure 1. Sketches of the Nematic, Smectic A and Smectic C liquid crystals.

aligned along a common direction denoted by a vector field **n** called director (Figure 1(a)). **n** is defined as a unit vector bearing no polarisation (i.e. **n** and –**n** are equivalent). The lack of positional order allows the nematic to flow like a liquid, but the orientational order confers anisotropic uniaxial optical properties (birefringence) and orientational elasticity. The bulk elastic distorsion of a nematic can be separated into three basic deformations, namely splay (**Δ.n**), twist (**n.Δ × n**) and bend (**n × Δ × n**) of the director. The energetic cost of these deformations was first derived by Frank and Oseen in a continuous description (*6, 7*):

$$\Delta F_{\text{Frank}} = \int d^3x \left\{ \underbrace{\frac{K_1}{2}(\nabla.\mathbf{n})^2}_{\text{splay}} + \underbrace{\frac{K_2}{2}(\mathbf{n}.\nabla\times\mathbf{n})^2}_{\text{twist}} + \underbrace{\frac{K_3}{2}(\mathbf{n}\times\nabla\times\mathbf{n})^2}_{\text{bend}} \right\}. \quad (1)$$

The elastic constants K_i have the dimension of an energy × (length)$^{-1}$ and are of the order of k_BT/(molecular length). The nematic phase is 'soft' enough that thermal fluctuations can excite long wavelength modes of large amplitude.

2.2 *The smectic A phase*

The next step towards more ordered mesophases is the condensation of the smectic A order when the continuous translational symmetry is broken along the director. The smectic A material is a one-dimensional periodic stack of liquid layers (Figure 1(b)). The periodicity is of the order of a molecular length, i.e. 2–4 nm. The layer normal **N** is parallel to the director: the smectic A phase (SmA) is uniaxial. The theoretical description of the N–SmA transition requires the identification of an order parameter. Following de Gennes and Prost (*5*) and McMillan (*8*), one can notice that the layered structure of the SmA phase is characterised by a periodic modulation of all the microscopic properties along the director **n**. The electron density, for instance, commonly probed by X-ray scattering, can be expanded in the Fourier series:

$$\rho(\mathbf{x}) = \rho_0 + \sum_{n=1}^{\infty} \psi_n\, e^{i\mathbf{q}_S.\mathbf{x}} + \psi_n^*\, e^{-i\mathbf{q}_S.\mathbf{x}}, \quad (2)$$

in which $\mathbf{q}_S = \mathbf{q}_S.\mathbf{n}$ is the wavevector of the smectic modulation. The fundamental term ψ_1 in the Fourier expansion in Equation (2) is obviously zero in the nematic phase. It is a natural choice for the N–SmA order parameter. It has two real independent component

$$\psi_1(\mathbf{x}) = \rho_1(\mathbf{x})\, e^{i\phi_1(\mathbf{x})}. \quad (3)$$

The modulus $\rho_1(\mathbf{x})$ measures the strength of the local SmA ordering and phase: the more segregated the molecules are into well-defined layers, the higher the ρ_1. Variations of the phase $\phi_1(\mathbf{x})$ are related to the local displacement $u(\mathbf{x})$ of the layers (with $\phi_1(\mathbf{x}) = -i\,\mathbf{q}_S\,u(\mathbf{x})$) and account for local compression $\Delta_{//}u$ and curvature $\Delta_{\perp}u$ of the layers (subscripts // and ⊥ denote directions parallel and perpendicular to the director respectively). The smectic A order parameter therefore has an XY symmetry.

2.3 *The smectic C phase*

In the smectic C phase (SmC) (Figure 1(c)), the director **n** and the layer normal **N** make a finite angle θ (**n.N** = cos θ). The direction of the projection **c** of the director on the plane of the layers defines the azimuthal angle φ. The SmC phase is then biaxial. The SmA–SmC order parameter is again of XY symmetry with two independent components θ and φ.

3. Chirality in liquid crystals

Chirality is the property of objects that are different from their mirror image. Experiments show that the introduction of chirality (chiral mesogen or chiral dopant) in a nematic phase generates a spontaneous twist of the director, for instance **n** = (cos $2\pi x/P$, sin $2\pi x/P$, 0) for a helical twist of pitch P along a direction x perpendicular to **n**. Such a twisted nematic phase, first found in cholesterol derivatives, is called cholesteric (or N*). The higher the chirality (i.e. the enantiomeric excess or the fraction of chiral dopant), the higher the twist (i.e. the shorter the pitch). Twist is thus the structural response induced by the microscopic chiral symmetry breaking, in agreement with the Curie principle. The covariant expression of the local twist, used in Frank energy Equation (1), is **n.**curl **n** (= $-2\pi/P$ in the example of the cholesteric helix).

A natural extension of the Frank energy density to chiral nematics is then (*5*)

$$\Delta F_{\text{Frank}}^{\text{Chiral}} = \int d^3x \left\{ \frac{K_1}{2}(\nabla.\mathbf{n})^2 + \frac{K_2}{2}(\mathbf{n}.\nabla \times \mathbf{n})^2 + \frac{K_3}{2}(\mathbf{n} \times \nabla \times \mathbf{n})^2 - h\,\mathbf{n}.\nabla \times \mathbf{n} \right\}, \qquad (4)$$

in which the field h coupled to the twist identifies with the chirality. In the mean field, the free energy of a chiral nematic $\Delta F_{\text{Frank}}^{\text{Chiral}}$ is the minimum ($= -h^2/2K_2$) for the helical solution of twist $k_0 = 2\pi/P = -h/K_2$: $\mathbf{n} = (\cos 2\pi x/P, \sin 2\pi x/P, 0)$ which satisfies $\boldsymbol{\Delta}.\mathbf{n} = 0$, $\mathbf{n} \times \text{curl}\,\mathbf{n} = \mathbf{0}$ and $\mathbf{n}.\text{curl}\,\mathbf{n} = -h/K_2$. Note that the pitch then gives a measure of the chirality h. The sign of h reflects the handedness of the helix.

In the defect-free smectic phases of layer thickness d and layer normal $\mathbf{N}$, the number of layers crossed along a path going from a point P_1 to a point P_2 is $\int_{P_1}^{P_2} \mathbf{dl}.(\mathbf{N}/d)$, independent of the path P_1P_2. This property implies curl $(\mathbf{N}/d) = \mathbf{0}$.

In a smectic A phase, the layer normal $\mathbf{N}$ identifies with the director field and d is a constant so that curl $\mathbf{n} = \mathbf{0}$: twist and bend cannot develop on macroscopic scales. The penetration of twist requires either a non-uniform layer thickness $d(\mathbf{x})$ (which can be achieved on a limited scale with the twist penetration depth λ_2 of the order of $\sqrt{K_2/B}$, in which B is the elastic modulus of compression of the smectic layers (*5*)) or defects, such as dislocations, which make the integral $\int_{P_1}^{P_2} \mathbf{dl}.(\mathbf{N}/d)$ path-dependent. In the mean field, $\mathbf{n}.\text{curl}\,\mathbf{n} = 0$ everywhere in the smectic A phase and Equation (4) implies that the free energy density of the cholesteric phase is decreased by the twist term $-h^2/2K_2$ with respect to the untwisted smectic A. The cholesteric to SmA transition becomes first order at a temperature T_{N^*A} lower than T_{NA}.

In a smectic C phase, the layer normal no longer coincides with the director field. Non-zero twist and bend (i.e. curl $\mathbf{n} \neq 0$) are permitted. The helical structure of the director is $\mathbf{n}(\mathbf{x}) = (\sin\theta \cos 2\pi z/P, \sin\theta \sin 2\pi z/P, \cos\theta)$ for a layer normal along z ($\mathbf{N}.\mathbf{n} = \cos\theta$).

4. The nematic to smectic A transition: analogy with superconductors

The description of the N–SmA transition is quite simple in the mean field approximation that neglects all spatial inhomogeneities. The order parameter is then considered as constant for the entire sample. In the vicinity of the N–SmA phase transition, a Landau free energy density may be expanded in invariant powers of the order of parameter ψ (subscript 1 will be omitted in the following). Translational invariance requires that the phase $\phi(\mathbf{x})$ does not enter the free energy. The Landau expansion hence reduces to

$$\Delta F_1 = \frac{r}{2}|\psi|^2 + \frac{u_0}{4}|\psi|^4 + \ldots, \qquad (5)$$

with $r = a(T - T_{NA})$ and $u_0 > 0$, the N–SmA transition is second order at the mean field temperature T_{NA}. The modulus $|\psi|$ grows as $(r/u_0)^{1/2}$ below T_{NA}. The critical exponent β of the order parameter is thus 1/2 as usual with mean field theories.

Because the smectic order is one dimensional, the fluctuations of the layers described by the local displacement field $u(\mathbf{x})$ are known to play an important role, even far away from any phase transition: the squared amplitude $\langle u^2(\mathbf{x})\rangle$ diverges like the logarithm of the size of the sample (the so-called Landau–Peierls instability (*9–11*)), hence killing true long-range order.

Close to the N–SmA transition, fluctuations of the amplitude ψ are also expected to be important. They are taken into account in a Landau–Ginzburg expansion of a local Hamiltonian. Once again, only even powers of $|\psi|$ are permitted. Including gradient terms and fluctuations of the nematic director $\delta\mathbf{n}_\perp = \mathbf{n}(\mathbf{x}) - \mathbf{n}_0$ ($\mathbf{n}_0 = \hat{z}$) yields the following Landau–Ginzburg functional:

$$\Delta F_{\text{N–SmA}} = \frac{1}{2}\int d^3x \left\{ r|\psi|^2 + \frac{u_0}{2}|\psi|^4 + C_{//}|\nabla_z\psi|^2 + C_\perp|(\nabla_\perp - iq_S\delta\mathbf{n}_\perp)\psi|^2 + K_1(\text{div}\,\delta\mathbf{n}_\perp)^2 + K_2(\hat{z}.\text{curl}\,\mathbf{n})^2 + K_3(\nabla_z\delta\mathbf{n}_\perp)^2 \right\}. \qquad (6)$$

The first two terms are the Landau part of Equation (5). Because of the nematic anisotropy, the gradient terms exhibit anisotropic coefficients ($C_{//} \neq C_\perp$) along directions parallel and perpendicular to the director $\mathbf{n}$. With the notation $\Delta_z = \partial/\partial z$ and $\Delta_\perp = (\partial/\partial x, \partial/\partial y)$ and at the lowest relevant order in $\delta\mathbf{n}_\perp$, these gradients have the form shown in Equation (6). The last three terms are the usual Frank–Oseen elastic energy of the nematic (expanded from Equation (1)).

If one forgets about the fluctuations of the director (i.e. set $\delta\mathbf{n}_\perp = 0$ in Equation (6)), the N–SmA problem becomes equivalent to the condensation of superfluid helium (the XY model in dimension $D = 3$; the anisotropy of the elastic coefficients $C_{//}$ and $C_\perp$ can be removed by a simple anisotropic rescaling).

With non-zero $\delta\mathbf{n}_\perp$, Equation (6) is very similar to the Landau–Ginzburg functional describing the normal–superconductor transition (*1, 5, 12*):

$$F = \frac{1}{2}\int d^3x \left\{ \alpha|\psi|^2 + \frac{\beta}{2}|\psi|^4 + \frac{1}{2m} \left| \left(\hbar\nabla - i\frac{2e}{c}\mathbf{A}\right)\psi \right|^2 + \frac{1}{4\pi\mu}(\text{curl } \mathbf{A})^2 \right\}. \quad (7)$$

Here, ψ is the superconductor gap order parameter. It corresponds to the wave function of the superconducting pair in BCS theory and has the same XY symmetry as the smectic order parameter. The magnetic vector potential **A** becomes analogous to the director field **n** (m and e are the mass and the charge of a single electron, $\hbar = h/2\pi$ is the Planck's constant, c is the velocity of light and μ is the magnetic permeability).

Comparing Equations (6) and (7) shows that curl **n** in LCs is analogous to the magnetic field **B** = curl **A**. Twist (**n**.curl **n**) and bend (**n** × curl **n**) are components respectively parallel and perpendicular to the director. The anisotropy of the two components of curl **n** follows from $K_2 \neq K_3$. An experimental bending field coupled to **n** × curl **n** only is not easy to realise. It would produce a spontaneous curvature of the director of the nematic. On the other hand, chirality h is a microscopic source of twist and identifies with the component of a vector field **h** (analogous to **H**) coupled to **n**.curl **n** (i.e. h = **h**.**n**). K_2 is then the permeability to twist. The cholesteric is then analogous to a normal metal in a magnetic field. Table 1 summarises the correspondence between superconductors and LCs through de Gennes' analogy.

Interesting behaviours of the smectic state can be deduced from the analogy:

Table 1. Correspondence between superconductors and LCs through de Gennes' analogy.

Superconductor	Liquid crystal
$\psi = \|\psi\|\exp(i\phi)$ = Cooper amplitude	$\psi = \|\psi\|\exp(iq_0u)$ = mass density wave amplitude
A = vector potenti	**n** = nematic director
H = magnetic intensity	h = molecular chirality
B = curl **A** = microscopic magnetic field	k_0 = **n**.curl **n** = twist
normal metal	nematic
normal metal in external field	cholesteric
Meissner phase	Smectic A phase
London penetration depth	twist penetration depth
coherence length ξ	smectic coherence length ξ_{Sm}
magnetic vortex	screw dislocation
Abrikosov vortex lattice phase	TGB (twist grain boundary) phase

- Just as superconductors expel the magnetic field curl **A** (the Meissner effect (*13*)), smectics expel twist and bend as the two components of curl **n**. Experiments confirm that the twist and bend moduli K_2 and K_3 diverge as they should upon approaching the smectic state from the nematic phase.
- Two important lengths characterise a superconductor, namely the order parameter coherence length $\xi = (m/|r|)^{1/2}$, over which ψ can vary and the London penetration depth of the magnetic field $\lambda = (mc^2/2\mu e^2|\psi|^2)^{1/2}$. Type I or type II behaviour depends on the value of the Ginzburg parameter $\kappa = \lambda/\xi$.
  - Type I ($\kappa < 1/\sqrt{2}$). The superconducting state is observed with perfect Meissner effect below a critical field H_c.
  - Type II ($\kappa > 1/\sqrt{2}$). Two critical values of the field are found. Vortices bearing a quantum flux $\phi_0 = \pi\hbar/e$ penetrate the material for $H < H_{c2}$ (upper critical field) and crystallise on a triangular lattice (the Abrikosov flux lattice). The Meissner phase condenses below the lower critical field $H_{c1} < H_{c2}$.

For smectics, two order parameter coherence lengths $\xi_{//,\perp}$ and four penetration lengths $\lambda_{//,\perp}^{2,3}$ associated with twist and bend can be identified, which precludes simple classification:

$$\xi_{//,\perp} = \left(\frac{C_{//,\perp}}{|r|}\right)^{1/2} \quad \lambda_{//,\perp}^{2,3} = \left(\frac{K_{2,3}u}{2C_{//,\perp}q_S^2|r|}\right)^{1/2}. \quad (8)$$

Although the Ginzburg parameter is not known for smectics, the superconductor analogy suggests two distinct behaviours. They are summarised in Figure 2. In the type II case, a mixed phase analogous to the Abrikosov flux phase should develop. Following the analogy, an appropriate molecular field could induce the penetration of bend or twist via a lattice of defects, just as magnetic flux penetrates a type II superconductor via a lattice of magnetic vortices. The penetration of bend via a lattice of edge dislocation was proposed in de Gennes' original paper (*1*). The external 'bending' field was defined as a macroscopic bend imposed by the surfaces of a wedged cell. It is, however, the penetration of twist that led to the spectacular demonstration of the fantastic superconductor analogy because the 'twisting' field (i.e. the molecular chirality) was easier to monitor experimentally than the 'bending' field.

Before we introduce the structure of the smectic analogue of the Abrikosov flux phase in the next section, let us point out that the bare smectic coherence

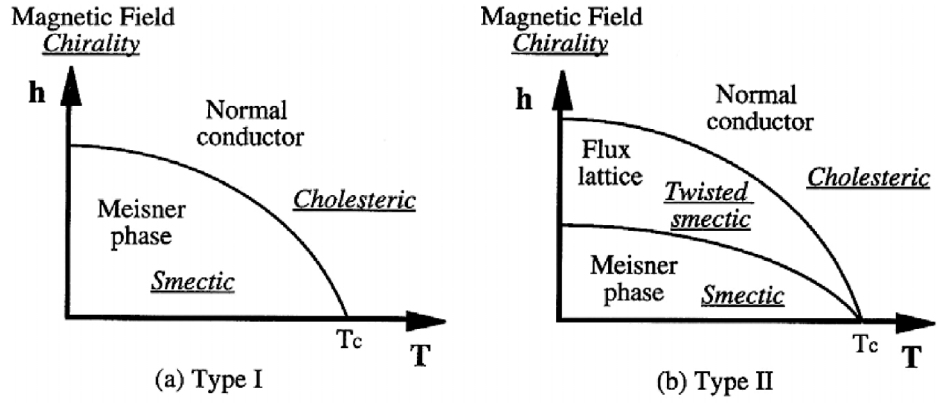

Figure 2. Temperature–field phase diagram for superconductors and liquid crystals for type I (a) and type II (b) conditions. The magnetic field h of the superconductor diagram is replaced by the chirality field in the liquid crystal case.

length at 0 temperature $\xi_0 = (C_\perp/aT_{NA})^{1/2}$ with $r = a(T - T_{NA})$ is significantly shorter than its superconductor equivalent (1–2 nm in metals instead of 500 nm) because of the higher value of the transition temperature T_{NA}. An interesting consequence deriving from the Ginzburg criterion is that the critical domain is expected to be much larger (i.e. more easily accessible) in the smectic case. Experiments confirm that the N–SmA transition does not exhibit simple mean field behaviour, unlike low T_c superconductors. We shall see in Section 7.2 that the effect of fluctuations bears similarities with high-T_c superconductors.

Another important difference between the worlds of superconductors and LCs is gauge invariance and the absence of true smectic long-range order.

The superconductor Hamiltonian (Equation (7)) is invariant under any gauge transformation, such as

$$\mathbf{A} \rightarrow \mathbf{A}' = \mathbf{A} + \Delta L \text{ and } \psi \rightarrow \psi' \exp(-q/cL), \quad (9)$$

in which L is an arbitrary scalar field.

In the smectic case, the Frank–Oseen energy is not gauge invariant because of the splay term $K_1.(\text{div } \delta\mathbf{n})^2$. The lack of gauge invariance reflects the fact that the director field **n** is a physical observable (unlike its magnetic vector potential analogue **A**). There is in fact only one physical gauge, namely $\delta n_z = 0$. Consequently, the behaviour of some physical observables, such as the correlation lengths, cannot be simply extrapolated from the superconductor model, but can be calculated from Gauge transformation theories (*14*).

5. The Renn–Lubensky model of the Twist Grain Boundary phase

Type I behaviour of the N–SmA transition has been commonly reported: a second order N–SmA transition observed at temperature T_{NA} in a racemic mixture of chiral compounds (i.e. at zero chiral field h) becomes first order at a lower temperature on the chiral enantiomer in agreement with Figure 2(a). Type II behaviour implies the existence of a mixed phase in which the twist penetrates the smectic structure. Its experimental search required more theoretical guidance. The light came from the theoretical work of Renn and Lubensky who were the first to propose the structure of the mixed phase – called the TGB phase or TGB – in 1988 (*3*). This is shown in Figure 3. The twist penetrates the TGB structure via a twisted lattice of screw dislocations analogous to magnetic vortices. Smectic slabs of constant thickness are regularly stacked along the pitch direction $\hat{x}$. Adjacent smectic slabs are separated by a grain boundary (GB) formed by parallel screw dislocations in a plane perpendicular to $\hat{x}$. The effect of each GB is to rotate the layer normal by a finite angle $\Delta\theta$ linked to the density of screw dislocations by

$$\frac{d}{2l_d} = \sin\frac{\Delta\theta}{2} \quad \text{and} \quad \frac{l_b}{P} = \frac{\Delta\theta}{2\pi} = \alpha, \quad (10)$$

in which l_d is the average distance between the screw dislocations in the GB and l_b is the width of a smectic slab.

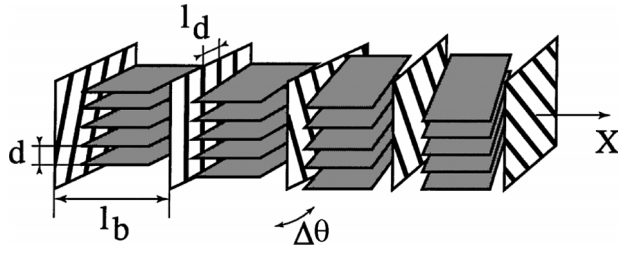

Figure 3. Structure of the TGB phase. The layers are represented, but not the molecules (from (*19*)).

The twist k ($\equiv 2\pi/P$) remains finite ($= k_{c2}$) at the upper critical field h_{c2} (i.e. cholesteric–TGB transition) with $k_{c2} = h_{c2}/K_2$, but vanishes at the lower critical field h_{c1} (cholesteric–SmA transition).

The reciprocal space structure of the TGB phase depends on the value of the ratio α.

- If α is irrational, the structure exhibits no periodicity (the so-called incommensurate TGB). The reciprocal space is a uniform ring of radius $q_0 = 2\pi/d$ in the plane q_y,q_z perpendicular to the pitch (Figure 4(b)). The profile along q_x is Gaussian proportional to $\exp(-q_x^2\xi^2)$ with ξ of the order of $(q_0 k_{c2})^{-1/2}$ (*3*).
- If α is rational ($\alpha = p/q$ with p,q mutually prime integers, the so-called commensurate TGB) the TGB structure is periodic of period $pP = q\ l_b$ along $\hat{x}$ with q-fold rotational symmetry. The reciprocal lattice is a series of rings of q equispaced Bragg spots in a discrete series of planes at $q_x = 0$ [$2\pi/pP$] (Figure 4(c)). The intensity of the rings falls off quickly with q_x as $\exp(-q_x^2\xi^2)$. If q differs from the crystallographic values (2, 3, 4 or 6) the commensurate TGB has a quasi-crystalline symmetry.

At this point, the superconductor analogy of de Gennes is completed by the Renn–Lubensky (RL) model, which offers a complete theoretical description of the first order (type I) or continuous (type II) nematic to smectic A transition when chirality is present. A subsequent theoretical question was about the relevance of the type II situation. Was there any chance to observe this fantastic TGB structure that had never been reported before, despite intensive work on LCs? Once again, theory proposed an answer to this question, hence providing the chemists and the experimental physicist with precious guidance (*15, 16*).

The flavour of the RL solution (*15*) can be understood from Equation (8). The transverse smectic correlation length $\xi_\perp$ and the penetration length $\lambda_\perp$ vanish and diverge, respectively at the SmA–SmC transition where $C_\perp$ vanishes. Consequently, the Ginzburg parameter κ is expected to diverge (at least its $\perp$ component) and the type II condition is to be fulfilled in the vicinity of a chiral NAC point where the N–SmA and the SmA–SmC lines meet. The exact theoretical phase diagrams were worked out in (*16*) and are shown in Figure 5. They involve three TGB phases with different smectic orders: the TGB_A phase with local SmA order as described above and two novel TGB_C and TGB_C* phases with local smectic C and helical smectic C* order, respectively. Three slightly different topologies were predicted for different values of the Frank elastic constants K_{1-3}, but all of them opened up a stable TGB phase in place of the chiral NAC point.

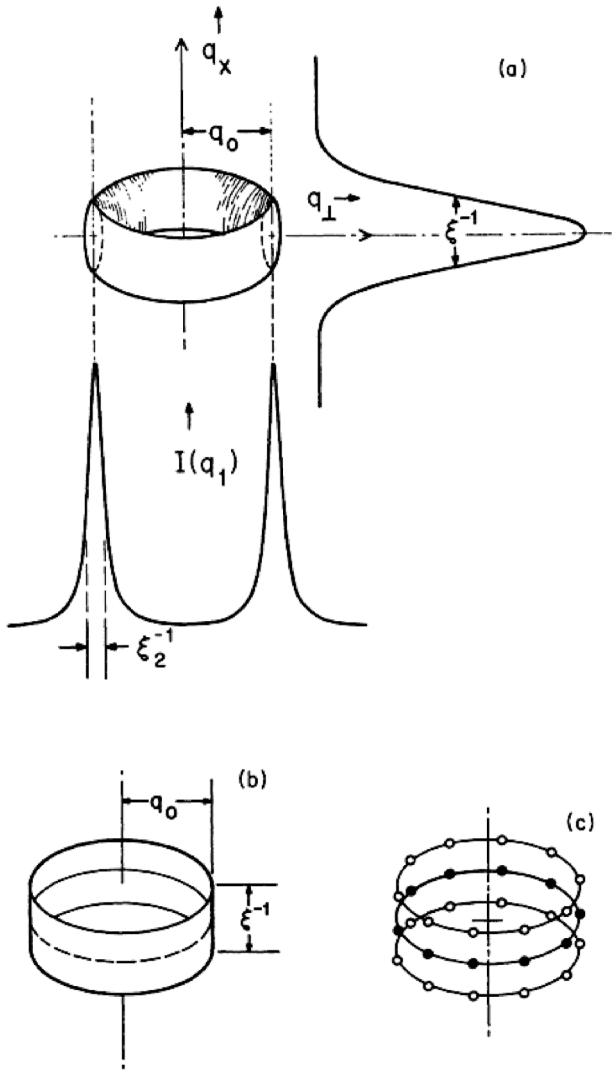

Figure 4. X-ray scattering intensity $I(\mathbf{q})$ calculated near the upper critical field h_{c2}: (a) $I(\mathbf{q})$ for the cholesteric phase just above h_{c2}. The scattering is intense on a torus obtained by rotating an oval centred at $q_z = q_0$ and $q_x = 0$ about the q_x axis. As a function of q_x at fixed $q_\perp$, $I(\mathbf{q})$ is a Gaussian of width $\xi^{-1} \approx (q_0\, k_{c2})^{1/2}$. As a function of $q_\perp$ at fixed q_x, it is a Lorentzian of finite width ξ^{-2}. (b) $I(\mathbf{q})$ in the TGB phase with α irrational. There is intense scattering on a cylinder of radius q_0 and height ξ^{-1}. (c) $I(\mathbf{q})$ in the TGB phase with $\alpha = p/q$. There are Bragg peaks at equally spaced spots on rings of radius q_0 in the y–z plane at $q_x = J\, k_0/p$. If q is even, there are q spots in each ring. If q is odd, there are $2q$ spots in each ring. The intensity of the spots die off as $\exp(-q_x^2\xi^2)$. In this figure, only the Bragg peaks on rings at $q_x = 0$ (closed circles) and $q_x \approx \xi^{-1}$ (open circles) are drawn (from (*3*)).

6. The experimental discovery of the TGB_A phase

Shortly after the publication of the RL model, the discovery of a TGB phase was reported by Goodby *et al.* (*17*) in a homologous series of ferroelectric chiral material. This new liquid crystalline phase

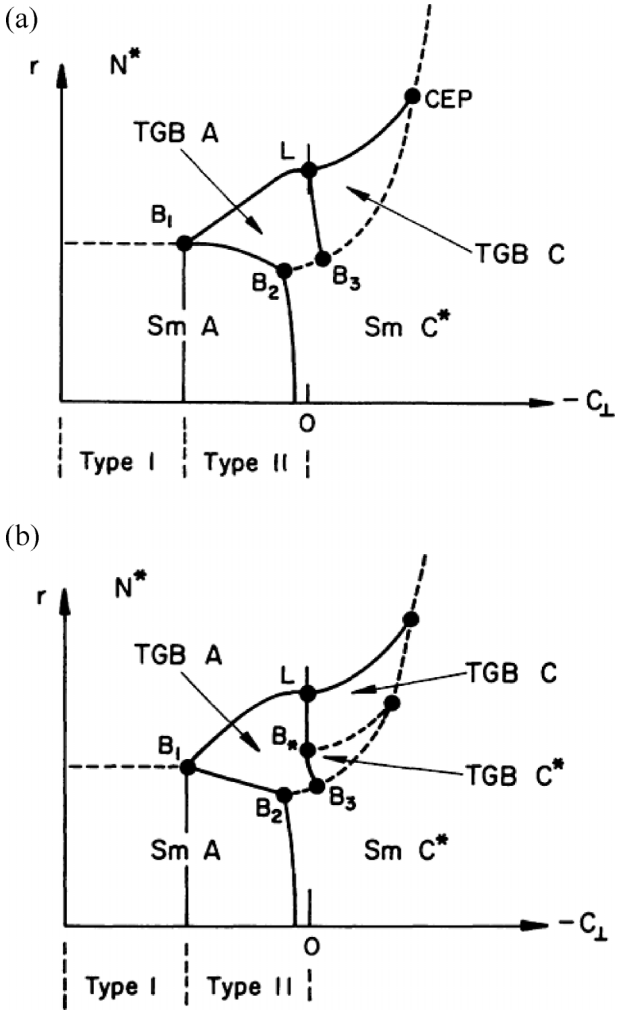

Figure 5. Theoretical phase diagram at the chiral NAC point. (a) If the Frank constants satisfy K_1 and $K_2 < K_3$, two TGB phases appear in the NAC region where the type II condition is met, namely TGB_A and TGB_C with local SmA and SmC order, respectively. Dashed and solid lines denote first and second order transition lines respectively. (b) If K_1 and $K_2 > K_3$, an additional TGB_C* phase appears with helical local SmC* order (from (*14*)).

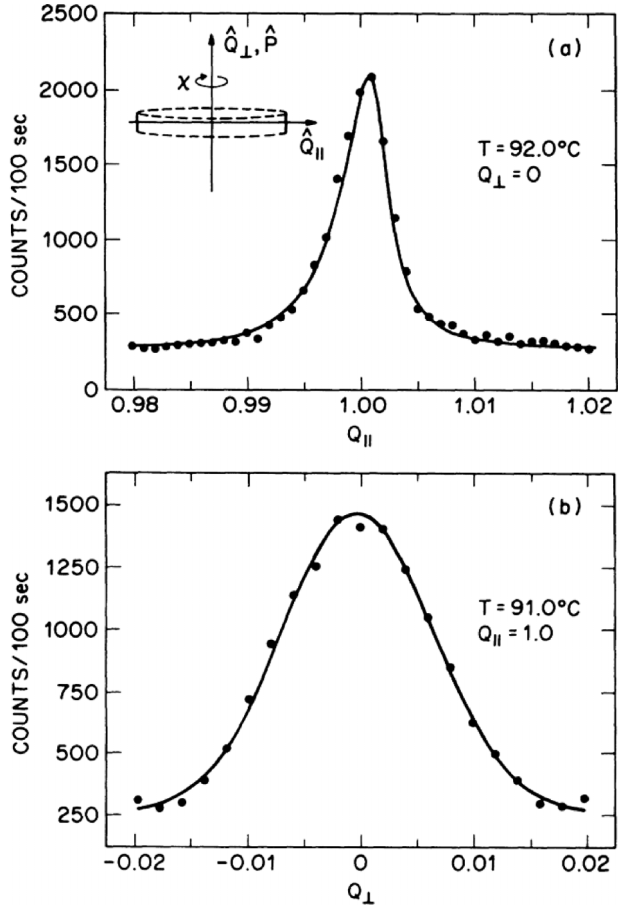

Figure 6. X-ray intensity scattered from a well-aligned TGB sample: (a) perpendicular to the helical axis along the radius of the Bragg cylinder; (b) along the helical axis through the Bragg cylinder at $q_{//} = q_0$ (reduced $Q_{//} = 1$). The solid line is a fit to a Gaussian function as predicted by the RL model (from (*18*)).

indeed combined the optical properties of a cholesteric and the X-ray signature of a smectic phase.

The structure of the new phase was first characterised by Srajer *et al.* (*18*) by optical and high resolution X-ray studies performed on oriented samples. The helical nature of the phase was demonstrated by selective reflection of circular polarised light. The helical pitch was found to decrease linearly from 0.63 to 0.38 μm with increasing temperature. The ring of scattering proposed by the RL model was fully characterised with a Gaussian line shape of characteristic width 0.033 $Å^{-1}$ along the pitch direction q_x (Figure 6). No evidence of commensurability was found in the circumference of the Bragg cylinder, so that the twist angle $\Delta\theta$ between adjacent dislocations could not be measured. The full set of the structural parameters could, however, be estimated from the reasonable assumption $l_b \approx l_d$, which yielded $l_b \approx 185$ Å and $\Delta\theta \approx 13°$.

The highly dislocated real space structure was demonstrated by freeze fracture experiments by Ihn *et al.* (*19*). Figure 7 shows the discontinuous change of orientation of the frozen smectic layers with respect to the plane of fracture and the cores of the screw dislocations, which appear as endpoints terminating abruptly the lines revealing the smectic steps.

At this point, only two years after the publication of the theory (*3*), it was clear from the optical, X-ray scattering and freeze fracture experiments reported above that the existence of a new liquid crystalline phase, fully consistent with the highly dislocated RL model of the TGB phase, had been demonstrated.

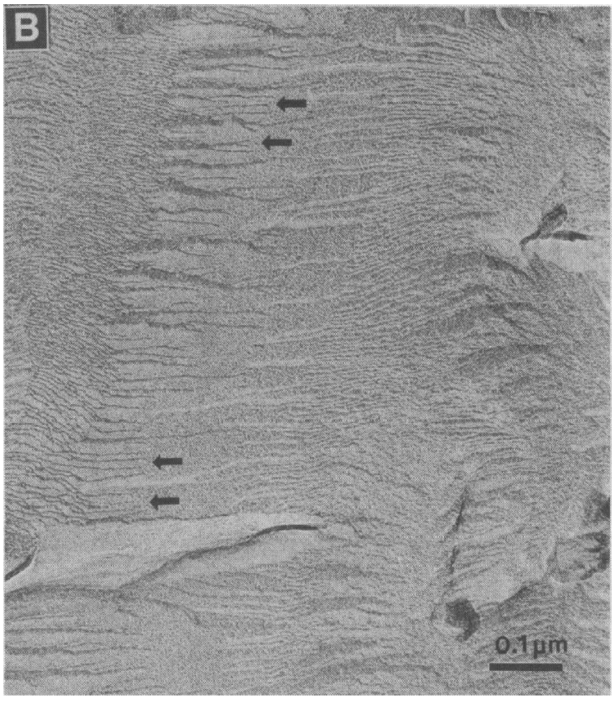

Figure 7. Freeze fracture image of typical screw dislocations in the TGB_A phase. The characteristic 'river' fracture pattern, which terminates abruptly at the defect core, is characteristic of screw dislocations (arrows). The screw dislocations form the TGBs that cause the orientation of the layers to change abruptly with respect to the fracture surface in roughly vertical bands from left to right (from (*19*)).

These pioneering results stimulated considerable interest and research efforts, as we will review below.

The direct observation of the discrete and constant rotation angle $\Delta\theta$ at thermal equilibrium came from X-ray scattering experiments on oriented samples. Figure 8(a) shows the discrete ring of scattering recorded on a TGB_A sample (*20*). According to the RL model, the figure corresponds to a commensurate TGB with a rational ratio $\alpha = 1/46$, i.e. a rotation angle $\Delta\theta = 2\pi/46 = 7.83°$. The number q of spots on the ring ($=1/\alpha$) is plotted versus temperature in Figure 8(b). In this case, the two lengths l_b and l_d are obtained independently from Equation (10). The inset of Figure 8(b) shows that the ratio l_b/l_d is almost constant and close to 1, which is in excellent agreement with the theoretical calculation within harmonic elasticity theory (*21, 22*).

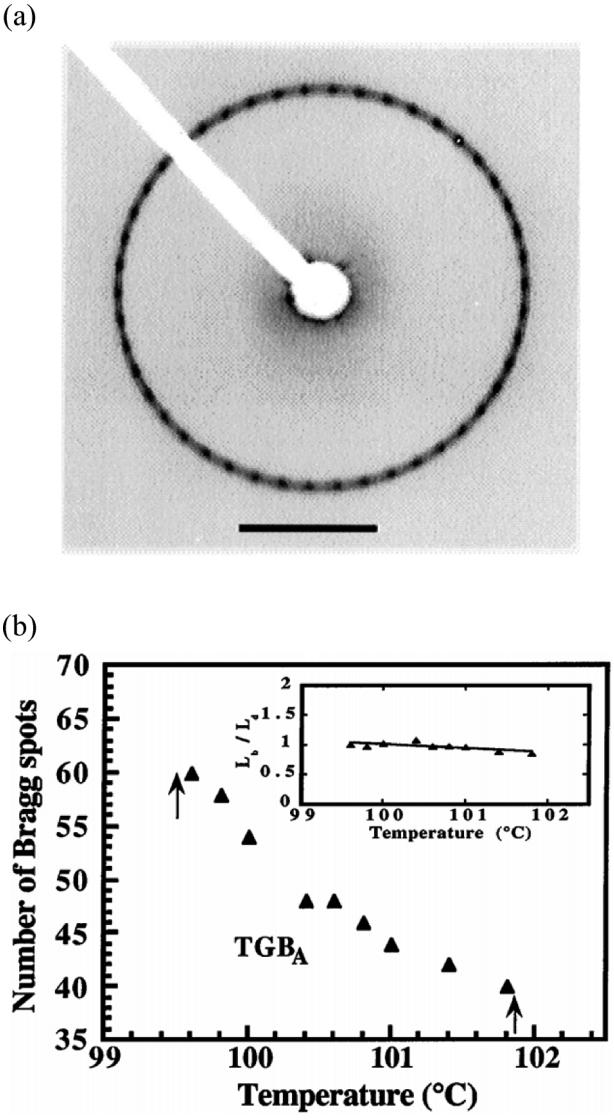

Figure 8. (a) Diffraction pattern of a well aligned TGB_A phase. The incident beam is parallel to the pitch axis. The ring of scattering exhibits 46 equispaced Bragg peaks. (b) Number of Bragg spots versus temperature. Inset shows that the ratio l_b/l_d is roughly constant and equal to 1 (from (*20*)).

7. Phase diagrams in thermotropic liquid crystals

7.1 The chiral NAC problem and the TGB_C phase

The experimental observation and characterisation of the TGB_A phase undeniably constituted a brilliant success of the RL model. However, the complete validation of the initial superconductor analogy required one to demonstrate the link with the type II condition. This fundamental demonstration was provided by the study of experimental phase diagrams and the identification of the TGB_C phase proposed by Lubensky and Renn (*15*) and Renn (*16*).

In order to investigate the vicinity of a chiral NAC point, Nguyen *et al.* (*23*) and Bouchta *et al.* (*24*) synthesised new chiral LCs combining cholesteric to smectic transitions and a smectic A to smectic C transition in the same series of chiral homologous compounds $n\mathrm{F_2BTFO_1M_7}$'. The topology of the experimental phase diagram, shown in Figure 9, exhibits a striking similarity with the theoretical diagram of Figure 5(a).

A new phase domain corresponding to the theoretical TGB_C phase opens up, surrounded by the cholesteric, smectic C* and TGB_A phases. The TGB nature of this new phase was revealed by the simultaneous observation of selective reflection of visible light (as in a cholesteric) and Bragg reflection of X-rays (as in a smectic phase). The microscopic structure of the TGB_C was fully characterised by the Bordeaux group by X-ray scattering from oriented samples (*25*). Figure 10 shows the X-ray profile along the component q_x, parallel to the pitch axis. The scattering, diffuse and centred at $q_x = 0$ in the cholesteric phase, sharpens and splits into two symmetrical peaks upon cooling in the TGB_C phase. The corresponding structure is shown in Figure 11. Unlike the TGB_A phase, the smectic C layers are tilted by an angle ω_L with respect to the helical axis. Hence, the reciprocal vectors lie on two cones at angle $\pm\omega_L$, relative to the symmetry plane q_y, q_z. Moreover, since the value of ω_L identifies with the value of the smectic C tilt, the director field **n**(**r**) remains perpendicular to the pitch axis, as in the TGB_A phases. A consequence is that the spontaneous polarisation $\mathbf{P}_S$ of the chiral smectic C slabs is also perpendicular to the pitch axis ($\mathbf{P}_S \propto \mathbf{n}.\mathbf{N}$) and precesses about it: the structure is hence 'heli-electric'. This structure differs from the TGB_C originally proposed by RL with non-tilted layers (*15*, *16*). Kundagrami and Lubensky (*26*) showed later that the free energies of the two TGB_C structures (i.e. RL and Bordeaux TGB_C) are actually very close.

The modulation of the scattering around the two cones enabled the direct measurement of the rotation angle $\Delta\theta = 2\pi/q$ across the grain boundaries. Values of q ranging from 18 to 20 (for the homologous compound $12F_2BTFO_1M_7$) and up to 26 (for $11F_2BTFO_1M_7$) were observed. The ratio l_b/l_d was found to be between 7.0 and 8.5, significantly larger than in the TGB_A phase (*27*) in agreement with Kundagrami and Lubensky (*26*).

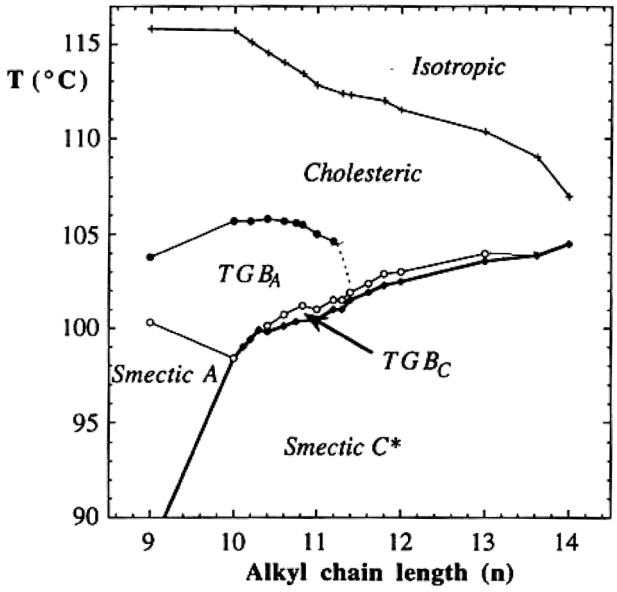

Figure 9. Experimental phase diagram showing the occurrence of the TGB phases in the chiral NAC system. Note the similarity of the topology with the theoretical diagram of Figure 5(a) (data from (*23*) and (*24*)).

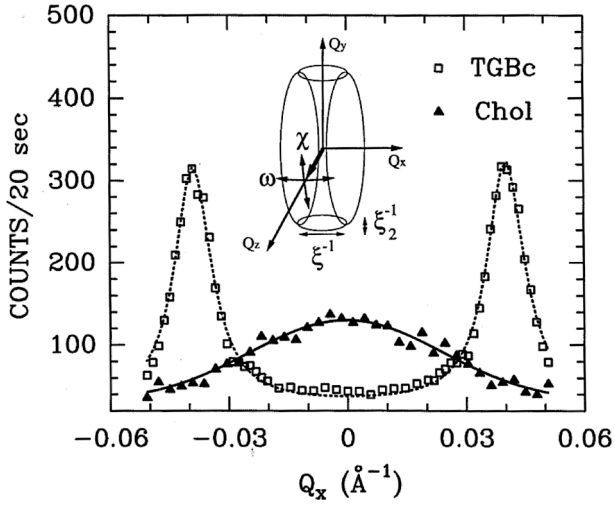

Figure 10. Plot of the X-ray intensity scattered along the direction q_x of the pitch axis through the Bragg maximum at $q_z = q_0$ for the $12F_2BTFO_1M7$ tolane compound exhibiting a direct cholesteric–TGB_C transition (from (*25*)).

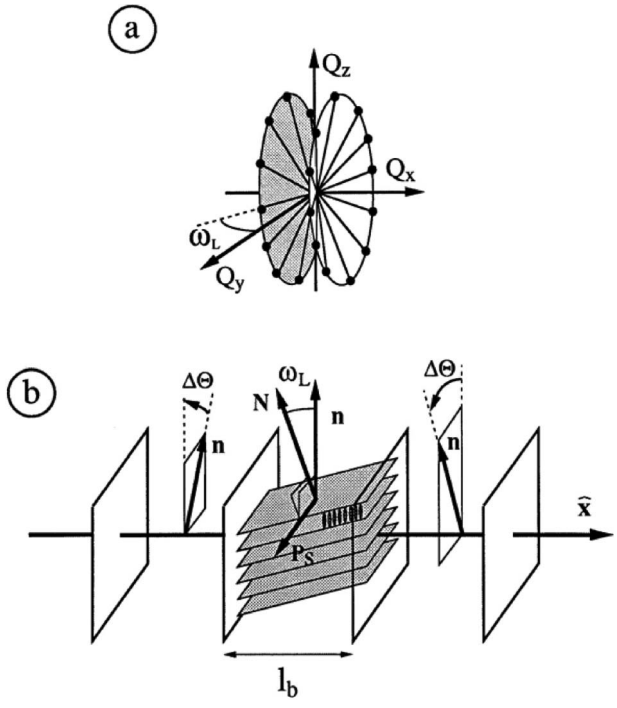

Figure 11. Structure of the TGB_C phase: (a) reciprocal space; (b) direct space representation. The smectic layers are tilted by an angle ω_L relative to the helical axis $\hat{x}$(from (*25*)).

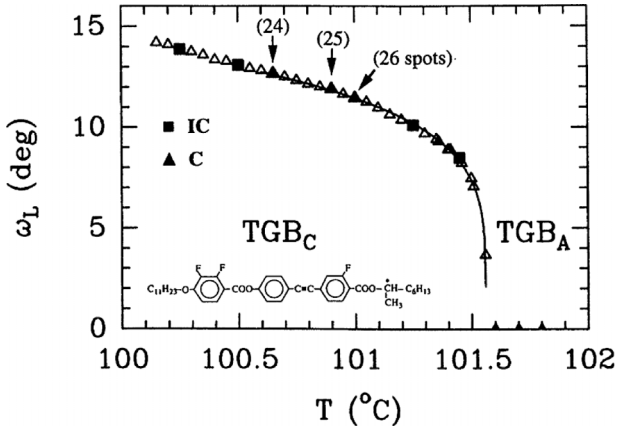

Figure 12. Tilt angle ω_L of the layers relative to the helical axis versus temperature at the TGB_A–TGB_C transition for the molecule shown. The best fit of the data to a power law behaviour $(T^* - T)^{\beta}$ yields $\beta = 0.20 \pm 0.05$ (solid line). Modulated (commensurate) and incommensurate angular scans are indicated by triangles and squares, respectively. The molecular structure of the material $11F_2BTFO_1M7$ is shown (from (*25*))

The study of the homologous compound $11F_2BTFO_1M_7$ is instructive as it reveals the behaviour at the TGB_A–TGB_C transition. Figure 12 shows that the tilt of the layers ω_L behaves like an order parameter with power law behaviour $(T^* - T)^{\beta}$ with $\beta = 0.20 \pm 0.05$.

7.2 The TGBC phase*

For some particular sets of the Frank elastic constants (K_1, $K_2 > K_3$), the theory of Renn (*16*) suggests the existence of an additional TGB phase in which the smectic C slabs have a local helical Smectic C* structures (TGB_C* phase, Figure 5(b)). Numerous experimental efforts have been devoted to the search and characterisation of the TGB_C* phase.

In 1997, Pramod *et al.* (*28*) reported the discovery of a new TGB phase in a binary mixture: the undulated TGBC* (U-TGBC*), characterised by the appearance of a translational symmetry-breaking square grid pattern in the plane normal to the helix axis, and by undulations, with displacement along the helix axis, of the grain boundaries of isolated TGB filaments. The model presented to explain these undulations (*29*) is a helical arrangement of tilted molecules within each SmC*-like block, similar to the Renn model of the TGB_C* phase. However, the presence of such a helix has not been confirmed.

In 1999, Ribeiro *et al.* (*30*) published results obtained with a single-component liquid crystalline material. By optical and structural X-ray studies, they characterised a TGB_C phase (S-TGB_C) exhibiting a square grid optical pattern in planar geometry and a very broad angular distribution of the layer normal (ω scans) relative to the TGB helix axis. This broad distribution profile can be interpreted either as a broad zero-centred Gaussian function (characteristic of a non-layer-tilted RL TGB_C structure) or with two broad overlapping maxima at $+\omega_L$ and $-\omega_L$, (characteristic of a TGB_C structure where the layers are tilted by an angle ω_L relative to the TGB helical axis $\hat{x}$). Galerne (*31*) proposed some complements to the Renn model of the TGB_C* phase, to explain the typical textures observed in oriented samples.

In 1993, Shao *et al.* (*32*) reported several new nitroalkoxy tolane LC materials with TGB phases over wide temperature ranges, including TGB_C phases. The TGB_C phase in one of these materials (W371, compound #9 in (*32*)) was later found to exhibit the RL layer structure, with layer normal **N** perpendicular to the helix axis, as well as the square grid modulation at low temperatures (*33*).

Recently, Fernsler *et al.* (*34*) studied a second compound in this family (W376, compound #8 in (*32*)). In aligned wedge-shaped samples with planar boundary conditions, optical studies in the W376 phase show, in addition to the classical Grandjean texture characteristic of a helical structure with the helical axis perpendicular to the glass plates, surprising hexagonal and square grid patterns (Figure 13). X-ray experiments made on the same sample gave various results. Firstly, the layer spacing, d, decreases when the temperature decreases. This is the proof of a tilted (smectic-C) like phase. The distribution of the layer normal (ω scan) is sharp and well zero-centred. This is characteristic of a RL TGB_C structure. Secondly, the scattering intensity recorded in the plane perpendicular to the TGB helical axis exhibits six equidistant spots (Figure 14), which is consistent with 3 or 6 smectic blocks per pitch, with the angle $\Delta\theta$ between two adjacent smectic slabs equal to 120 or 60 degrees, respectively. Additional studies by freeze fracture experiments showed that these features arise from a common structure of 'giant blocks' of thickness $l_b > 200$ nm, terminated by sharp grain boundaries mediating large angular jumps ($60° < \Delta < 90°$) in layer orientation between blocks, and lubricating the thermal contraction of the smectic layers within the blocks (Figure 15). This phenomenology of 'giant block' TGB (GBTGB) is well described by basic theoretical models (*34*), applicable in the limit that the ratio of molecular tilt penetration length-to-layer coherence length is large, and featuring grain boundaries with weak smectic ordering, approaching thin, melted (nematic-like) walls. In this limit the energy cost of change of the block size is small, leading to a wide variation of block dimensions, depending on preparation conditions. The

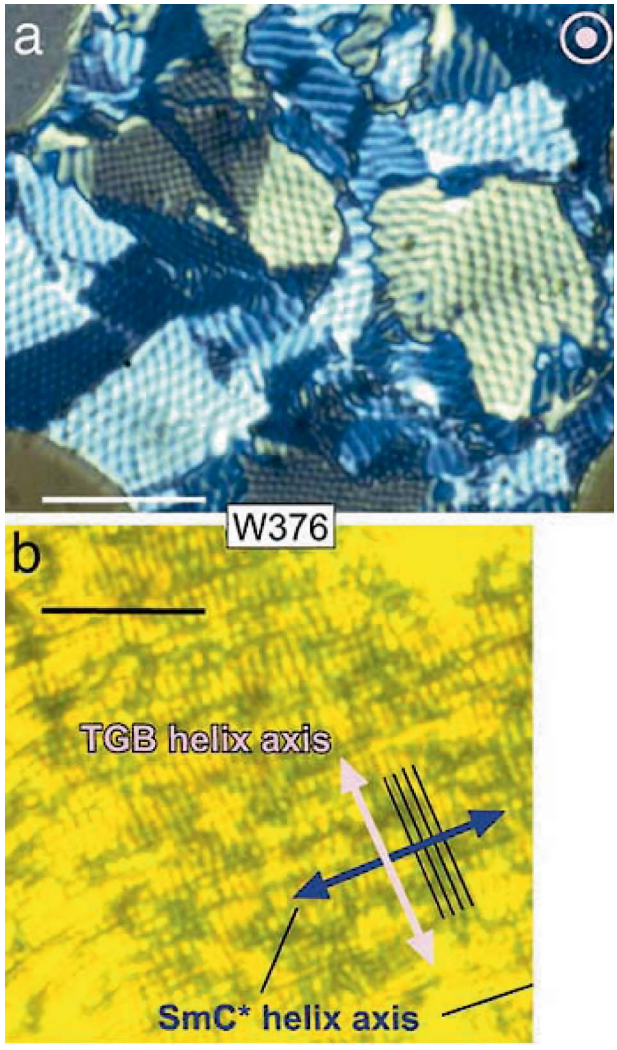

Figure 13. Polarised light micrographs of the TGB_C phase of GBTGB for the W376 material (transmission). The TGB helix axis is indicated in white and the SmC helix in blue. (a) Grandjean texture of a 2 μm thick cell in the $GBTGB_C$ phase, showing areas of 60° and 90° periodicity. (b) Planar-aligned with the TGB and SmC helices in the plane of the cell plates, showing orthogonal quasiperiodic arrays of lines from both helices. (Scale bars: 20 μm, (a) and (b)) (from (*32*)). Colour refers to the online version.

models also account for the temperature dependence of the TGB helix pitch.

To conclude this section, let us point out that other models of twisted smectic C phases have been proposed by Dozov and Luk'yanchuk, namely the Melted Grain Boundary (MGB) phase in which the grain boundaries are melted walls instead of screw dislocation walls (*35*) and the TGB_{2q} phase, which appears as the superposition of two degenerated TGB_C phases with different left and right layers inclinations (*36*). However, despite the persistence of a few open questions, the topological connexion of the TGB problem with the chiral NAC

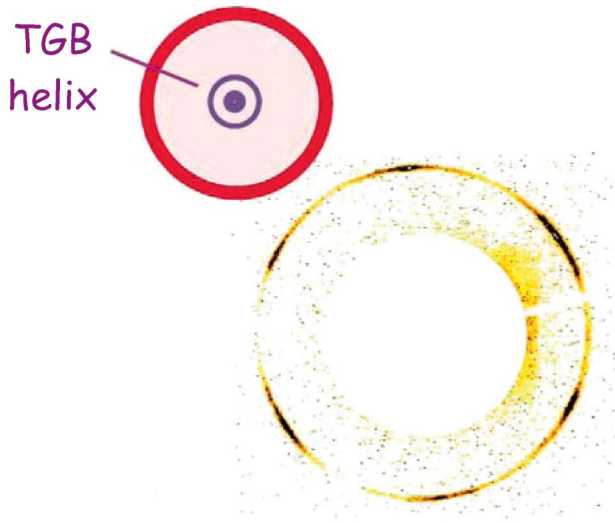

Figure 14. Structural features of GBTGB phase for the W376 material. Two-dimensional detector image of the angular distribution of intensity about the TGB helix axis for the W376 material. The sample is a monodomain exhibiting commensurate lock-in at 60° (from reference (*34*)).

point is clearly established, which strongly supports the link with the type II condition and therefore the superconductor analogy.

7.3 The fluctuations and the vortex liquid phase

Since the revelation of the superconductor analogy by de Gennes, high-T_c superconductors have been discovered and extensively studied (for a review, see for instance (*37*)). High-T_c superconductors are essentially type II and, unlike low-T_c superconductors, their critical domain is broad and the effects of the fluctuations are important. In this respect, the TGB phases are more closely related to high-T_c superconductors through the analogy. Thermal fluctuations can cause the regular Abrikosov lattice to melt, hence producing the entangled flux liquid in which the flux lines are, on average, parallel to a common direction (*38*). Dissipation occurs when an applied electric field produces flux flow, unless vortex pinning generates a disordered but static vortex glass phase (*39*).The observation of the LC analogue of the disordered vortex states (liquid or glass) would constitute further strong evidence of the importance of the analogy. Kamien and Lubensky (*40*) have proposed a structure for the LC vortex-liquid phase in which the screw dislocations exhibit no long-range positional order, but are arranged in a helical fashion to form a cholesteric LC. We use the subscript L to denote this new twisted phase N_L*. As in the SC case, it is important to notice that the N_L* phase locally has the order parameter of

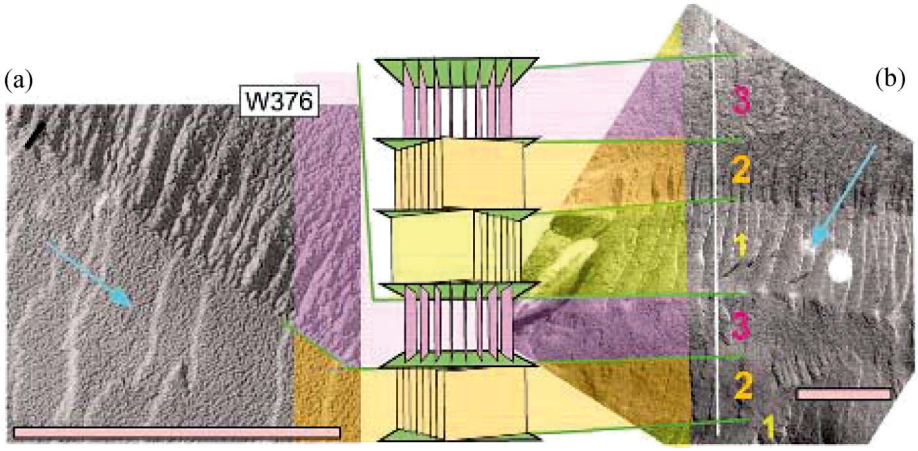

Figure 15. Freeze fracture electron microscopy (FFEM) images of the W376 compound, with sketches of the corresponding GBTGB layer structures. The material exhibits regions of three-block (60°) periodicity. The white arrow indicates the direction of the TGB helix, with the blue arrow showing the effective illumination direction for shadowing of the surface topography. MGBs are labelled with green lines. The scale of each image is indicated with a 400-nm-long pink bar. (a) Fractured at 50°C in the TGBC phase showing the MGB, the 40-nm-long black line is clearly significantly larger than the MGB width. (b) 60° structure in its TGBC phase (from (*34*)).

the low-temperature phase (i.e. smectic), but the macroscopic symmetry of the high-temperature phase. This model implies, of course, that the finite correlation length ξ_{Sm} of the smectic order parameter is larger than the average distance between the disordered screw dislocations: the very notion of screw dislocations becomes meaningless otherwise.

High-resolution calorimetric studies have first been used to investigate the phase diagram of several LC series exhibiting a SmA-TGB_A-cholesteric sequence (*41, 42*). The calorimetric data are consistent with the existence of the N_L* phase in an intermediate region between the TGB_A and the cholesteric phase: the broad intense peak detected in the heat capacity measurement above the TGB_A phase can be interpreted as a supercritical evolution from N_L* to a conventional cholesteric (see Figure 16). X-ray synchrotron studies reported in (*20*) showed that the local smectic order remains strong above the TGB_A phase, which is consistent with the disordered state of the Kamien–Lubensky model (*40*), but also with a simple TGB_A–cholesteric transition as described in (*3*).

More recently, two experimental approaches strengthened the Kamien–Lubensky model of the N_L* phase. Dynamic light scattering was used to probe the fluctuation modes in a TGB structure (*43*). In this work, the development of the TGB order at the cholesteric to proposed N_L* phase transition is revealed by an anomalous temperature dependence in the fluctuation spectrum and an instability in the helicoidal director structure.

High resolution X-ray diffraction was used to perform accurate measurements of the smectic correlation length ξ_{Sm} (*44*). The data of (*44*) show that ξ_{Sm} is finite but larger than the average distance l between screw dislocations in the N_L* phase. ξ_{Sm} decreases upon heating until the N_L*–cholesteric transition occurs when ξ_{Sm} becomes of the same order as l.

In conclusion to this section, it is undoubtedly fascinating to realise through the studies reported above the depth of de Gennes' analogy: most of the physical behaviours known in the world of superconductors have a confirmed counterpart in the world of LCs.

8. Physical properties of TGB phases

Although smectic phases exhibit a very simple crystallographic order, their physical behaviour is far from trivial. The destruction of true long-range order by the Landau–Peierl instability or the propagation of transverse modes of undulations (so-called 'second sound') are examples of complex physical properties of smectics (*1*). Since TGB phases are complex structures based on twisted stacks of smectic slabs, their physics is indeed expected to be even more complex. The theory of elasticity of TGB phases, for example, has been worked out by Toner (*45*) for the case of α irrational. It implies that fluctuations destroy long-ranged translational order, leading to algebraic (rather than δ-function) singularities in the X-ray scattering near both the Bragg cylinder in reciprocal space and isolated Bragg peaks along its axis. These results could be experimentally tested through high-resolution X-ray scattering, which, to our knowledge, has not yet been done.

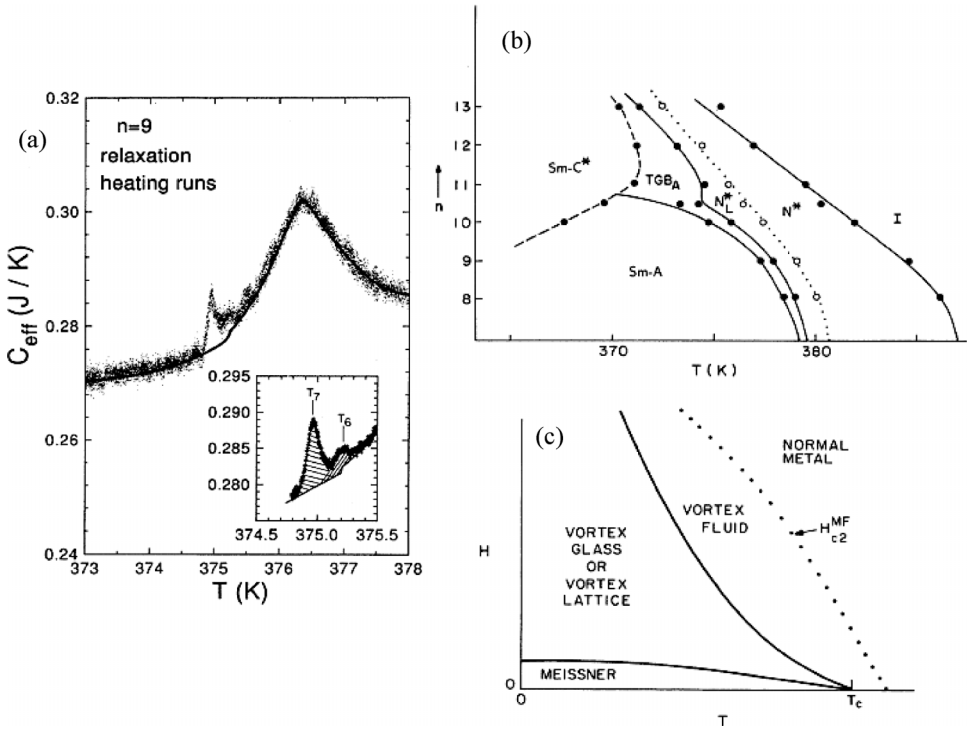

Figure 16. (a) High resolution measurement of the heat capacity of the compound 9FBTFO$_1$M$_7$. The broad feature at $T = 376.4$ K is the supercritical N_L*–N* evolution, not a true transition. The inset shows a detailed view of the SmA–TGB$_A$–N_L* region. (b) Phase diagram obtained by high-resolution calorimetry for the chiral series nFBTFO$_1$M$_7$ ($n = 8$–13). (c) Theoretical phase diagram for a type II superconductor with strong thermal fluctuations. Solid lines indicate first order transitions (from (*41*)).

In this section, we will restrict our attention to a selection of some physical properties of the TGB phases that have been experimentally observed.

8.1 Unwinding by an electric field

In the Abrikosov flux phase, the application of an electric field induces a superconducting current, which in turn creates a force on the magnetic vortices. The LC equivalent of applying a force on the screw dislocations of the TGB lattice is not exactly feasible. The effect of an external electric field **E** is nonetheless interesting in the case of TGB$_C$ structure, as it couples to the spontaneous polarisation of the chiral smectic C slabs and enables one to check the heli-electric model proposed in Section 7.1. The electric energy term f_i per unit area of the i^{th} slabs (Figure 11(b)) reads

$$f_i = -\int_{block} \mathbf{P}_S.\mathbf{E}\, dx = -P_S E\, l_{bi} \cos\chi_i, \qquad (11)$$

where l_{bi} is the i^{th} slab thickness and χ_i is the angle between the spontaneous polarisation $\mathbf{P}_{Si}$ and the electric field direction, chosen along y. In order to minimise the electric energy (Equation (11)), three different mechanisms are possible: (i) a modulation of the thickness l_{bi} of the slabs: according to the sign of their electric energy, slabs with positive (resp. negative) $\cos\chi_i$ will expand (shrink); (ii) a rotation of the slabs about the screw axis x under the effect of the electric torque in order to increase $\cos\chi_i$; and (iii) a modulation $\delta\mathbf{P}_{Si}$ of the modulus $\mathbf{P}_{Si}$ of the local polarisation. The first two effects have been observed and characterised in TGB$_C$ phases (*46, 47*).

Figure 17 shows the evolution of the scattered x-ray intensity around the TGB$_C$ cone in reciprocal space.

The third effect (iii) corresponds to an electroclinic distorsion and is expected to be strong close to the TGB$_A$–TGB$_C$ transition line. In the TGB$_C$ phase, the electric polarisation $\mathbf{P}_{Si}$ of slab i is proportional to $\mathbf{n}_i \times \mathbf{N}_i = \sin\theta_i$. An external field **E** parallel to $\mathbf{P}_{Si}$ will increase the local polarisation by increasing the tilt angle θ_i. This is the well-known electroclinic effect. Its magnitude is proportional to the component $E\cos\chi_i$ of the field along $\mathbf{P}_{Si}$. It is thus expected to be modulated with χ_i. A similar behaviour occurs for the TGB$_A$ phase, which has no spontaneous polarisation since $\mathbf{n}_i \times \mathbf{N}_i = 0$. The tilt and the polarisation are induced by the field in this case. Both should be likewise modulated by the helical structure of the TGB$_A$.

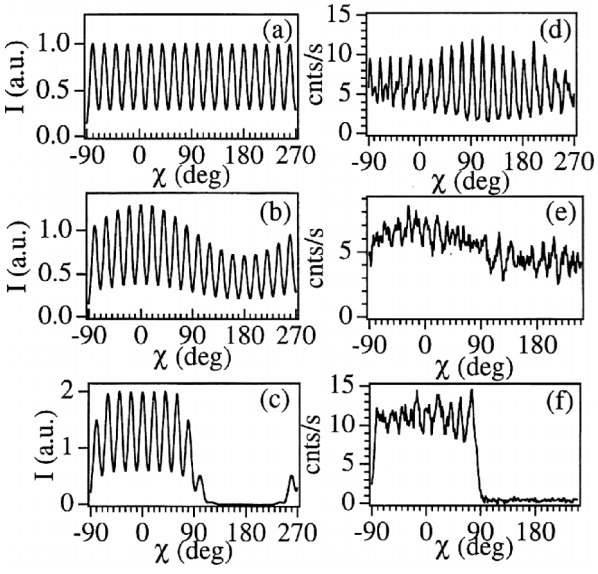

Figure 17. Simulated (a–c) and experimental (d–f) X-ray diffraction scans around the cone of the reciprocal lattice of a TGB_C phase under a transverse DC electric field (from (*47*)).

The local tilt θ_i can *a priori* be changed by reorienting $\mathbf{n}_i$, $\mathbf{N}_i$ or both. A rotation of the director $\mathbf{n}_i$ out of the y–z plane costs a large elastic energy of bend. The reorientation of $\mathbf{N}_i$ is, therefore, expected to prevail, allowing an easy detection by X-ray diffraction.

The experimental study of the modulated electroclinic effect in TGB phases was actually carried out by X-ray diffraction on oriented samples (*48*). The angular shift of the layer normal induced by the field is shown in Figure 18(a) (TGB_A phase) and Figure 18(b) (TGB_C phase). The dependence of the effect on field strength and temperature is displayed in Figure 19(a). It is well reproduced by a simple phenomenological model of elastically coupled grain boundaries at the TGB_A–TGB_C transition (Figure 19(b)).

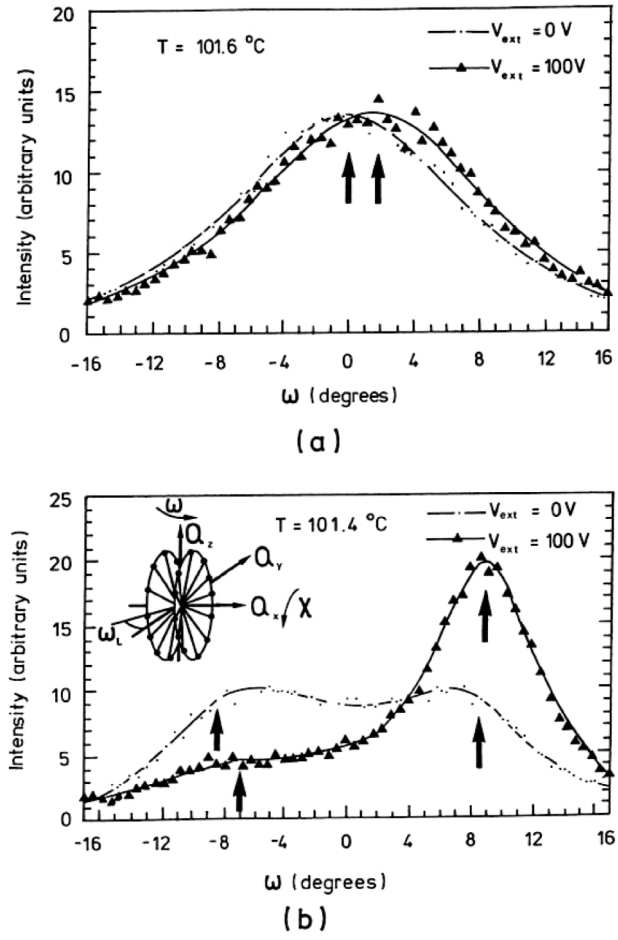

Figure 18. Rocking curves (ω-scans) recorded at constant wavevector transfer $\mathbf{Q}$ across the ring of scattering in the plane (Q_x,Q_y) perpendicular to the direction E_z of the applied electric field for external voltage equal to 0 and 100 V. (a) In the TGBA phase: at zero field (dots) the scattering is well fitted to the TGB Gaussian lineshape (solid line) centred at $\omega = 0$. In the field (diamonds) the Gaussian profile is preserved, but shifted by 1.8° (electroclinic effect). (b) In the TGBC phase: at zero field (dots), the profile exhibits two maxima centred at $\omega_L = \pm$ 8.5°. It is reasonably well fitted to two overlapping Lorentzian functions (solid line). In the field (diamonds) the two maxima are shifted both in intensity and angular position. The variation of the intensity is due to field induced translation of the grain boundaries. The inset shows the scattering geometry (from (*48*)).

8.2 Optical characterisation

We showed in the previous sections that the full characterisation of the highly-dislocated structure of the TGB phases and of the array of screw dislocations required the conjunction of several experimental techniques, namely the selective reflection of light (*4*), freeze fracture experiments (*19*) and the scattering of X-rays (*18, 20*). In a first approach, it seemed that the optical properties of a TGB structure were so close to the optics of a cholesteric helix that the two phases could not be distinguished under a classical optical polarising microscope. This is actually not quite true. Figure 20 shows a photograph of a sample with a co-existing cholesteric (bottom right corner) and a TGB_C (top left) taken with an optical microscope in a Cano wedge with weak planar anchoring (*49*). Two series of defect lines are visible. The usual array of Grandjean–Cano lines corresponding to edge dislocations of the helix is present in the two phases (large arrows). The larger spacing of the Grandjean–Cano lines in the TGB_C phase denotes a larger pitch. A series of additional lines,

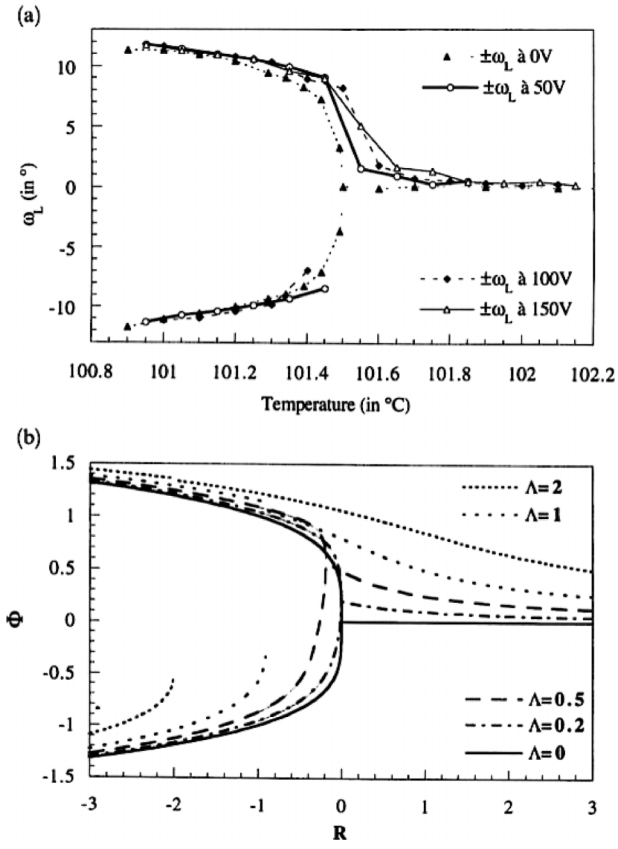

Figure 19. Tilt ω_L of the layers relative to the helical axis in the presence of an applied electric field: (a) experimental results; (b) numerical simulations (from (*48*)).

Figure 20. Optical microphotograph of a TGB_C sample in a wedge with planar anchoring between crossed polarisers. A $\lambda/4$ plate is inserted. The photograph size is $220 \times 330\ \mu m^2$. The TGB_C phase coexists with the cholesteric phase visible in the south-east corner. A series of parallel lines (small arrows) appears in the TGB_C phase only, in between the usual Grandjean–Cano steps (large arrows). These new defects are interpreted as edge dislocations of the layered array of smectic slabs forming the TGB structure (from (*49*)).

parallel to the Grandjean–Cano, are visible in the TGB_C phase only (small arrows). These new defects are interpreted as edge dislocations of the layered array of smectic slabs (or equivalently grain boundaries) forming the TGB structure. These new 'slab-dislocation' lines are also observed in the TGB_A phase. Their contrast is often improved if a quarter-wave plate is inserted.

A Grandjean–Cano line corresponds to an increase of the thickness of the wedged sample by a half-pitch. If the number of TGB slabs in a pitch is q, the number of 'slab-dislocations' between two adjacent GC lines should be of the order of $q/2$. A simple elastic model developed in (*49*) shows that the actual number depends on the elastic parameters of the structure and is always lower than $q/2$. Moreover, these characteristic lines appear in the thinnest region of the wedge only, below some critical thickness of the order of 4 to 6 half-pitches.

Their observation, which is inexpensive and easy, is a fast and safe way to characterise a TGB phase.

8.3 Commensurability

The commensurability of the TGB structures is a fascinating aspect of the theories and a somewhat controversial experimental question. The rational or irrational nature of the structural ratio $\alpha = 2\pi/\Delta\theta$ is fascinating because commensurate TGB can be quasi-periodic, and the physics of commensurate–incommensurate transitions may exhibit curiosities, such as Devil's staircase behaviour (see, for instance, (*50*)). The experimental observation of a commensurate lock-in is controversial because finite size effects may alter the interpretations (*51*). Indeed, the uniform ring of scattering of an incommensurate TGB may exhibit periodic modulations in a sample of limited thickness (i.e. if the number of smectic slabs is not high enough

to fill the ring of scattering). Furthermore, a thin enough sample will always display spots on the ring of scattering, regardless of its commensurate or incommensurate nature. The response to the commensurability question thus requires a well aligned sample of 'infinite' thickness, which for experimental physicists means a number of helical pitches much larger than unity or else an average intensity on the ring of scattering much larger than the intensity scattered by each smectic slab. This condition is generally only marginally satisfied on real TGB samples for which the thickness cannot be very much larger than 25 μm to warrant a good alignment.

The relationship between commensurability and thickness was investigated in a wedged cell in synchrotron experiments with a microfocussed X-ray beam (*52*). The TGB_C LC was illuminated with a 20×40 μm^2 beam and simply moved in the beam to change the thickness D in the wedge. The diffraction patterns, recorded on an area detector, are shown in Figure 21. In the thinnest part of the wedge ($D < 8$ μm, 0–4 pitches, zone 1), the diffraction peaks of the individual smectic slabs can be identified. A new series of Bragg spots appears for each additional pitch. The Bragg peaks of pitch $(n + 1)$ do not superimpose on the peaks of pitch n, which is the signature of an incommensurate stack. In the intermediate region ($8\ \mu m < D < 18\ \mu m$, zone 2), the distribution of Bragg peaks is almost uniform, again suggesting the growth of an incommensurate structure. In the thickest region ($18\ \mu m < D < 23\ \mu m$), the Bragg spots are too numerous to be individually distinguished, but a new angular symmetry emerges from their statistical distribution: the spots merge into a small number of equispaced broad maxima and build up a q-fold modulation of the intensity of the ring of scattering. The whole set of data is presented in Figure 22.

Interestingly, the commensurate aspect of the scattering is absent in thin samples and appears for higher thicknesses when the effect of surface anchoring and restricted geometry diminishes. These observations suggest that the investigated TGB_C sample is truly commensurate and that its q-fold symmetry results from a statistical distribution of the orientation of the smectic slabs over the whole sample, rather than from a true replication of the orientation at each period. The confirmation of this picture would require the investigation of higher thicknesses. Unfortunately, the quality of the alignment deteriorates above 23 μm, which precludes a more definite conclusion.

9. Other TGB-like phases and structures

The discovery of the TGB phases in rod-like thermotropic mesogens has stimulated research of similar structures in other types of LCs. The generation of a macroscopic twist in chiral polymer and lyotropic systems has been extensively studied, with a particular emphasis on the structure of chiral defects. A few important results are reviewed in this section.

9.1 Polymer systems

GB morphologies in lamellar diblock copolymers were characterised using transmission electron microscopy (TEM) (*51–53*). Two types of twist grain boundaries were observed in which the microphase separation of the two blocks was maintained in the GB region by intermaterial dividing surfaces that approximate classically-known minimal surfaces. The geometry of these interfaces was demonstrated by comparing experimental TEM images with ray tracing computer simulations of the model surfaces. The two morphologies observed were found to have intermaterial dividing surfaces that approximate either Scherk's first (doubly periodic) surface or a section of the right helicoid. The helicoid section boundary was observed at low twist angles, less than or equal to about 15°. The Scherk's surface family of boundary morphologies, which consists of a doubly periodic array of saddle surfaces, was found over the entire twist range from 0 to 90°. As the twist angle approaches 0°, the Scherk's surface GB morphology is transformed into a single screw dislocation that has a single helicoid as intermaterial dividing.

The lamellar diblock twist boundary morphologies share some structural characteristics of the TGB_A phase. In the TGB phase the grain boundaries occur with a regular periodicity and are an integral part of the equilibrium phase. The grain boundaries observed in diblock copolymers are metastable defects instead of thermodynamically-stable structures, and they occur with a random distribution throughout the material. However, the geometric requirements of joining lamellar layers across a concentrated region of twist reorientation are shared by both the diblock twist boundaries and the TGB phase.

Smectic ordering has been observed in perfectly monodisperse poly(γ-benzyl α,L-glutamate) (PBLG), which was synthesised using recombinant DNA technology. These PBLG molecules form rigid α-helical rods 11.45 nm in length. An experimental study (*56*) by TEM and electron diffraction reveals a banded morphology with a period of approximately 120 nm, which provides strong evidence for helical rotation of the director field, as in a cholesteric or a twisted smectic. Detailed examination of the relative orientation of the banding in the morphology images and the reflections in the electron diffraction patterns, indicating interchain and intrachain correlations, leads to the conclusion that the structure observed is a twisted smectic

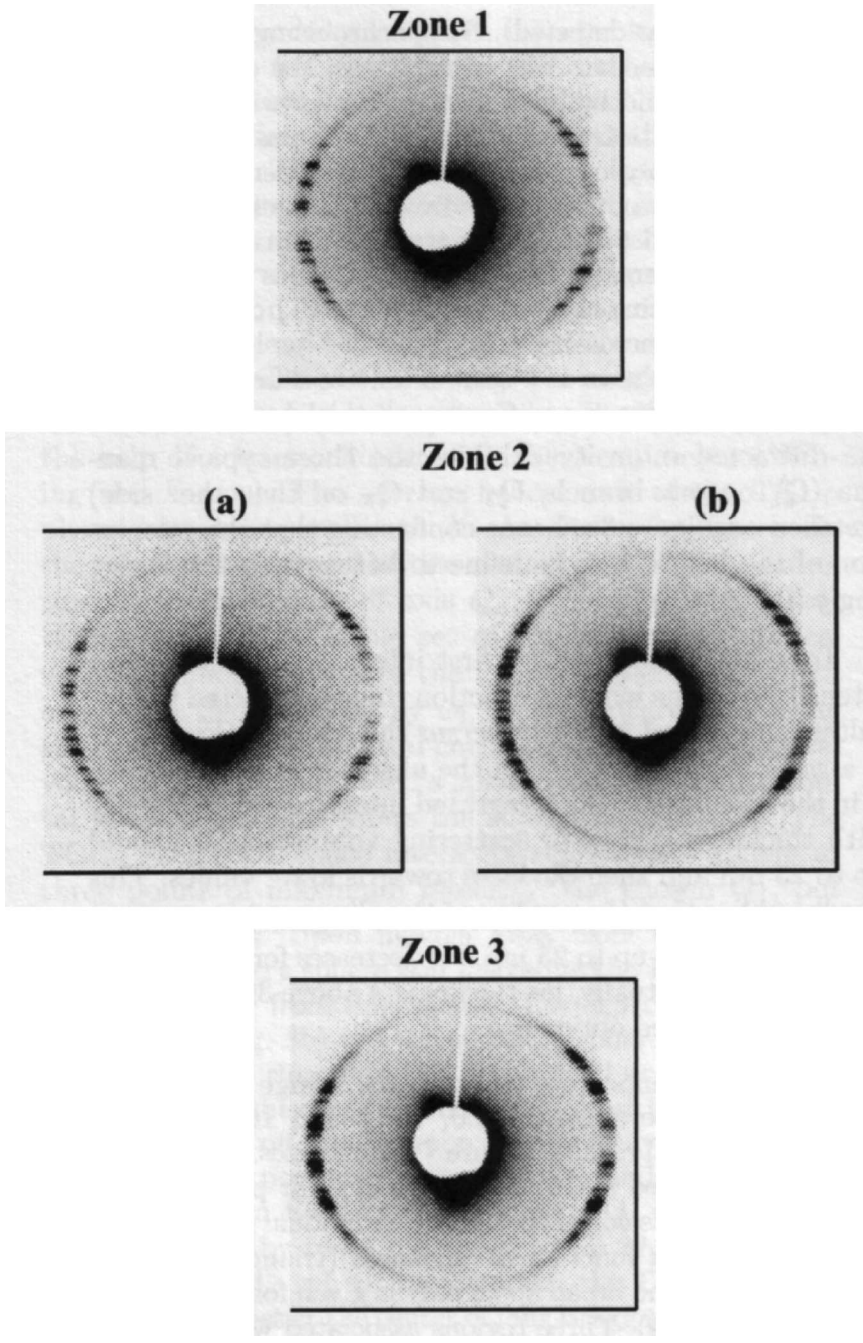

Figure 21. Diffraction patterns recorded at four different thicknesses D in the TGB_C phase. Zone 1: $D = 7.5\ \mu m \approx 3$ pitches. Each recorded spot corresponds to one single smectic C slab. The rectangular shape is due to the horizontal divergence of the focussed X-ray beam. The distribution of Bragg spots in bunches of three (corresponding to pitch numbers 1, 2 and 3) is clearly visible in the south-west quarter of the ring. The incommensurate twist angle $\Delta\theta$ is of the order of $2\pi/22 + 2\times10^{-3}$ *rd*. Zone 2: (a) $D = 9\ \mu m \approx 4$ pitches. Individual Bragg spots begin to evenly fill the ring. (b) $D = 18\ \mu m \approx 9$ pitches. The ring is almost uniformly filled as for an incommensurate distribution. Zone 3: $D = 21\ \mu m \approx 11$ pitches. The two numerous spots cannot be individually distinguished. A 20-fold modulation of the intensity appears (from (*52*)).

phase. The relationship between the twist and the layering is found to be that of a TGB phase. However, the data do not permit one to determine whether the monodisperse PBLG structure is made of blocks with discrete twist boundaries, as in a true TGB, or is a more continuously twisting structure. Thus, the authors refer to the phase as TGB-like. Conventional, polydisperse PBLG is well known for forming cholesteric phases as a result of the chirality of the helical rod. The formation of a TGB-like phase in monodisperse

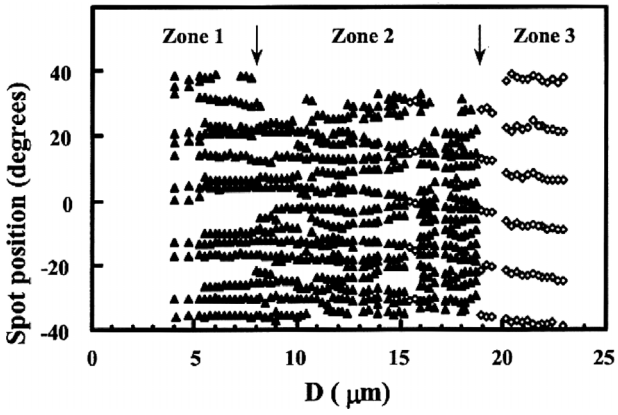

Figure 22. Plot of the angular position of the observed spots versus thickness of the sample in the wedge. Triangles denote individual Bragg spots diffracted by single smectic slabs, whereas diamonds correspond to the centre of the broad maxima of diffraction (from (*52*)).

PBLG is consistent with the superposition of a smectic-A layering resulting from the uniform rod length on the twisted texture present in the cholesteric. PBLG forms a cholesteric mesophase in a wide variety of organic solvents. The cholesteric twist of PBLG is dictated by the chirality of the α-helical macromolecules and the dielectric properties of the medium and cholesteric order can be retained in solution-cast solid films. There is no barrier preventing the transition from a cholesteric to a TGB-like smectic phase; the phase thus formed would preserve the director twist characteristics of the cholesteric. However, formation of a twisted smectic mesophase for conventional PBLGs is often hindered by the polydispersity of the chains.

9.2 Lyotropic LCs

In lyotropic lamellar systems, it is believed that because the molecules are amphiphilic, the molecular axes will align along the layer normal in an untilted L_α phase. In chiral lyotropic systems, there is a frustration between this normal alignment and the tendency of the molecules to twist (*57*). In 1997, Kamien and Lubensky (*58*) described a screw dislocation structure for lyotropic lamellae and proposed the existence of an L_α TGB phase. They also discussed a possible defect mediated phase transition between the L_α phase and a normal cholesteric.

They first model the free energy of an isolated bilayer membrane and consider the interactions between identical membranes. When such membranes are stacked together, they can form multi-layered, lamellar structures, similar to smectic-A phases in thermotropic LCs. In highly swollen systems, the layer spacing d is determined by entropic repulsion (*59, 60*). As in thermotropic smectics, the non-dislocated L_α phase excludes twist. Likewise, a sufficiently strong chirality can favour the penetration of twist into the L_α phase in the form of a TGB phase.

Transitions in lyotropic systems are driven predominantly via changes in concentration rather than changes in temperature. Kamien and Lubensky determined the surfactant concentration, or equivalently the layer spacing d, at which the L_α phase first becomes unstable with respect to a proliferation of dislocations by calculating the point at which the total energy per unit length of dislocation first becomes negative. In general, a transition occurs when d is reduced to twice the preferred Burger's vector of the free membrane. Possible phase diagrams are shown in Figure 23.

Kamien and Lubensky propose that the layers melt via dislocation loop unbinding, as in the smectic A–nematic transition (*61, 62*). Here, however, the chiral bias will cause one handedness of screw dislocation to be preferred over the other. This bias should change a second-order-like unbinding transition to a first-order transition: microscopic defect loops can no longer unbind smoothly since a loop must contain an equal number of left- and right-handed screws. Either the defect loops will unbind and the dissident part of the loop will move to the boundary, or, equivalently, the appropriate dislocations will nucleate from the boundary.

In 2006, Moreau *et al.* (*63*) report for the first time the direct observation, using freeze-fracture TEM, of topological melting in a lyotropic system in the vicinity of a smectic–cholesteric (N*) phase transition. The proliferation of dislocations leads to at least

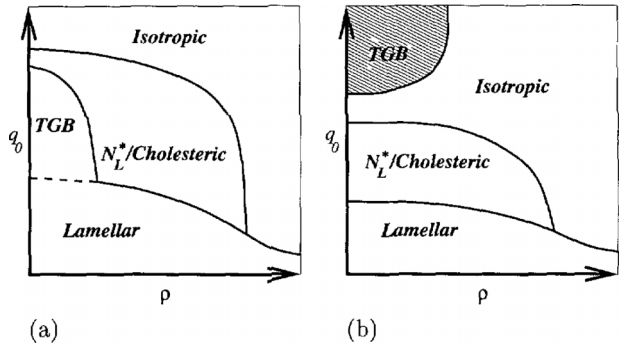

Figure 23. Possible phase diagrams for the lyotropic system as a function of chirality q_o and surfactant density ρ. Solid lines indicate first-order transitions while dashed lines indicate second order (or weakly first-order) transitions. (a) Lyotropic with four distinct phases: lamellar, TGB, N^*_L and isotropic. (b) It is possible that the isotropic phase intervenes before the TGB phase occurs. The phantom TGB region is shown with hatched lines: it will never appear (from (*58*)).

one, and possibly two, intermediate phases, characterised by orientational ordering of the dislocation loops (Figure 24). Close to the L_α–N* transition temperature (T = 19°C), dislocation loops are organised in a spatially-modulated two-dimensional structure (Figure 25(a)). Loops still display parallel long axes, but are now located in roughly equidistant planes. Several fully unbound zones have been observed (insert of Figure 25(a)). Unbound screw dislocations create twist walls (*64*) (two of them are displayed in Figure 25(b)), where the stacking direction of the layers abruptly turns. This organisation is strongly reminiscent of the structure of thermotropic TGB phases. The existence of TGB-like domains is therefore a strong indication for a type-II smectic. However, the authors do not know yet whether the organisation seen in FFTEM corresponds to a macroscopic phase or to local order only. Presently, it is their assumption that the spatially modulated organisation of the loops (Figure 25(a)) is induced by the macroscopic twist of a TGB-like state. This must be checked by working on non-chiral samples exhibiting a nematic phase instead of the N*/TGB phases. As stated by Kamien and Lubensky, lyotropic TGB

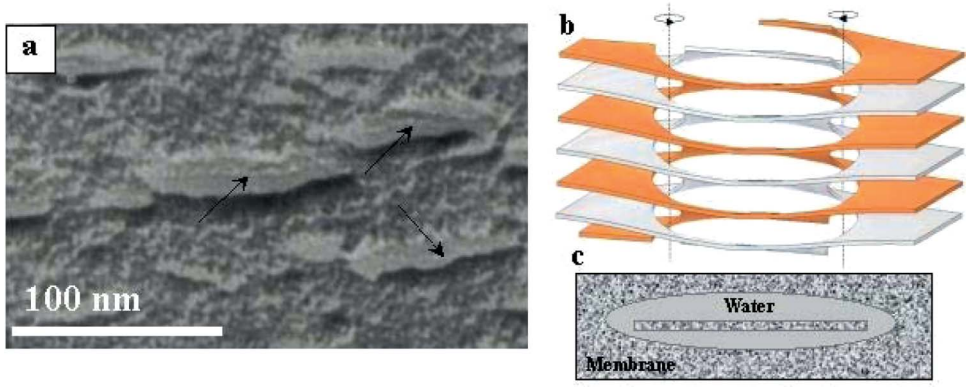

Figure 24. Dislocation loops. (a) Freeze fracture transmission electron microscopy (FFTEM) morphology of the defects at high magnification and T = 24°C. The texture inside the defects is smoother than outside. A thin white line can be observed in the defects parallel to their long axis (arrows). (b) Schematic representation of a dislocation loop of Burgers vector of magnitude two. Dotted lines indicate the axis of the two screw dislocations. Only membranes are represented. (c) Freeze fracture morphology expected if the fracture occurs in the layer plane (from (*63*)).

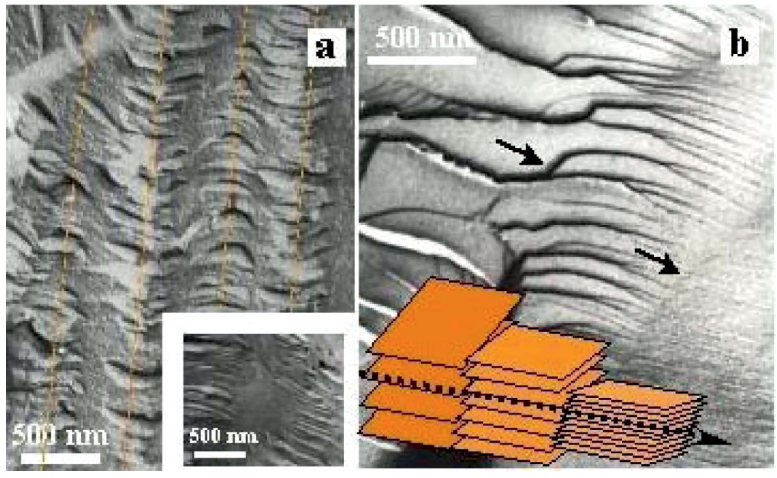

Figure 25. FFTEM images of the DMPC*sn*/C12E5/H2O (*Rs*/*l* = 2.8) system at 19°C. (a) Spatially modulated structure of the defected smectic at the L_C–N* phase transition. Dislocation loops organise in equidistant planes. Insert: zone of unbound dislocations. (b) Helical structure of the smectic phase at the L_C–N* transition. The orientation of the layers turns abruptly at each twist wall (arrows). Schematic representation of the TGB structure made of three smectic blocks separated by two twist walls (from (*63*)).

phases should mostly be liquid lines (N_L*). The exact nature of the TGB state (TGB_A, TGB_C, N_L* . . .) still needs to be characterised using X-ray scattering on oriented samples.

10. Conclusion

The fantastic success of the TGB story demonstrates the power of the superconductor analogy proposed by de Gennes in 1972. This success was undeniably triggered by the theoretical work of Renn and Lubensky in 1988: their model of the TGB phase constituted a decisive step forward for the community of chemists and experimental physicists, as it provided the necessary theoretical support to the concept of twisted layered structures. It is amazing to realise how much experimental and theoretical work followed in all types of LCs, from short thermotropic molecules to polymers and lyotropic systems.

So far, the analogy worked essentially in one way: from superconductors towards LCs. We reviewed in this paper how much the physics of TGB phases benefited from the physics of superconductors, but we have no example of progress going the other way. One may wonder if the study of TGB phases could in return benefit the physics of superconductors. This may seem unlikely if one considers that the research efforts and resources devoted to the study of superconductors are much higher than their TGB counterpart. It may be worth noting, however, that the physical observables are different in the two systems. The profile of the order parameter for instance, is easier to measure in LCs since the Fourier components of the smectic order parameter are directly probed by X-ray scattering.

Finally, let us mention the decisive importance of a contribution that de Gennes always acknowledged, namely the strong research efforts in chemical engineering and synthesis of new liquid crystalline materials. We mostly focused this review on the physics of the TGB phases, with very little emphasis on the design of molecules and systems. It is certainly fair to stress here that this beautiful physics owes a large part of its impact to the synthesis of original molecules.

References

(1) de Gennes, P.G. *Solid State Commun.* **1972**, *10*, 753–756.
(2) Domb, C.; Green, M.S., Eds.; *Phase transitions and critical phenomena*; Academic Press: London, 1976; Vol. 6.
(3) Renn, S.R.; Lubensky, T.C. *Phys. Rev. A* **1988**, *38*, 2132–2147.
(4) Goodby, J.W.; Waugh, M.A.; Stein, S.M.; Chin, E.; Pindak, R.; Patel, J.S. *Nature* **1989**, *337*, 449–452.
(5) de Gennes, P.G.; Prost, J. *The Physics of Liquid Crystals*, 2nd Edn.; Oxford Science Publication, Clarendon Press, 1993.
(6) Oseen, C.W. *Trans. Faraday Soc*. **1933**, *29*, 883–889.
(7) Frank, F.C. *Disc. Faraday Soc*. **1958**, *25*, 19–28.
(8) McMillan, W.L. *Phys. Rev. A* **1971**, *4*, 1238–1246.
(9) Landau, L.D. *Phys. Z. Sowj. Un.* **1937**, *2*, 26.
(10) Peierls, R.E. *Annls Inst. H. Poincarré*, **1935**, *5*, 177–222.
(11) Caillé, A. *C. R. Acad. Sci. Paris* **1972**, *B274*, 891–892.
(12) Ginzburg, V.L.; Landau, L.D. *J. Exptl. Theoret. Phys. (USSR)* **1950**, *20*, 1064–1082.
(13) Meissner, W.; Ochsenfeld, R. *Naturwiss*. **1933**, *21*, 787–788.
(14) Lubensky, T.C.; Dunn, S.G.; Isaacson, J. *Phys. Rev. Lett.* **1981**, *47*, 1609–1612.
(15) Lubensky, T.C.; Renn, S. *Phys. Rev. A* **1990**, *41*, 4392–4401.
(16) Renn, S.R. *Phys. Rev. A* **1992**, *45*, 953–973.
(17) Goodby, J.W.; Waugh, M.A.; Stein, S.M.; Chin, E.; Pindak, R.; Patel, J.S. *Nature* **1989**, *337*, 449–452.
(18) Srajer, G.; Pindak, R.; Waugh, M.A.; Goodby, J.W.; Patel, J.S. *Phys. Rev. Lett*. **1990**, *64*, 1545–1548.
(19) Ihn, K.J.; Zasadzinski, J.A.N.; Pindak, R.; Slaney, A.J.; Goodby, J.W. *Science* **1992**, *258*, 275–278.
(20) Navailles, L.; Pansu, B.; Gorre-Talini, L.; Nguyen, H.T. *Phys. Rev. Lett.* **1998**, *81*, 4168–4171.
(21) Bluestein, I.; Kamien, R.D.; Lubensky, T.C. *Phys. Rev. E* **2001**, *63*, 061702–061712.
(22) Bluestein, I.; Kamien, R.D. *Europhys. Lett.* **2002**, *59*, 68–74.
(23) Nguyen, H.T.; Bouchta, A.; Navailles, L.; Barois, P.; Isaert, N.; Twieg, R.J.; Maaroufi, A.; Destrade, C. *J. Phys. II France* **1992**, *2*, 1889–1906.
(24) Bouchta, A.; Nguyen, H.T.; Navailles, L.; Barois, P.; Destrade, C.; Bougrioua, F.; Isaert, N. *J. Mater. Chem.*, **1995**, *5*, 2079–2092.
(25) Navailles, L.; Pindak, R.; Barois, P.; Nguyen, H.T. *Phys. Rev. Lett.* **1995**, *74*, 5224–5227.
(26) Kundagrami, A.; Lubensky, T.C. *Phys. Rev. E* **2003**, *68*, 060703–060706(R).
(27) Navailles, L.; Barois, P.; Nguyen, H.T. *Phys. Rev. Lett.* **1993**, *71*, 545–548.
(28) Pramod, P.A.; Pratigha, R.; Madhusudana, N. *Curr. Sci.* **1997**, *73*, 761–765.
(29) Pramod, P.A.; Hatwalne, Y.; Madhusudana, N.V. *Liq. Cryst.* **2001**, *28*, 525–533.
(30) Ribeiro, A.; Barois, P.; Galerne, Y.; Oswald, L.; Guillon, D. *Eur. Phys. J*. **1999**, *B11*, 121–126.
(31) Galerne, Y. *Eur. Phys. J*. **2000**, *E3*, 355–368.
(32) Shao, R.; Pang, J.; Clark, N.; Rego, J.; Walba, D. *Ferroelectrics* **1993**, *147*, 255–262.
(33) Clark, N.A.; Shao, R.F. University of Pennsylvania TGB Symposium, Philadelphia; 1999.
(34) Fernsler, J.; Hough, L.; Shao, R.-F.; Maclennan, J.E.; Navailles, L.; Brunet, M.; Madhusudana, N.V.; Mondain-Monval, O.; Boyer, C.; Zasadzinski, J.; Rego, J.A.; Walba, D.M.; Clark, N.A. *PNAS* **2005**, *40*, 14191–14196.
(35) Dozov, I. *Phys. Rev. Lett.* **1995**, *74*, 4245–4248.
(36) Luk'yanchuk, I. *Phys. Rev. E* **1998**, *57*, 574–581.
(37) Burns, G. *High Temperature Superconductivity*; Academic Press Inc.: Boston, 1992.
(38) Nelson, D. *Phys. Rev. Lett.* **1988**, *60*, 1973; Nelson, D.; Seung, H. *Phys. Rev. B* **1989,** *39*, 9153–9174.
(39) Fisher, D.; Fisher, M.; Huse, D. *Phys. Rev. B* **1990**, *43*, 130; Huse, D.; Fisher, M.; Fisher, D. *Nature*, **1992,** *358*, 553–559.

(40) Kamien, R.; Lubensky, T.C. *J. Phys. I*, **1993**, *3*, 2131–2138.
(41) Chan, T.; Garland, C.W.; Nguyen, H.T. *Phys. Rev. E* **1995**, *52*, 5000–5003.
(42) Navailles, L.; Garland, C.W.; Nguyen, H.T. *J. Phys. II* **1996**, *6*, 1243–1258.
(43) Adorjan, A.; Stojadinovic, S.; Sukhomlinova, L.; Twieg, R.; Sprunt, S. *Phys. Rev. Lett*. **2003**, *90*, 035503–035506.
(44) Ybert, C.; Navailles, L.; Pansu, B.; Rieutord, F.; Nguyen, H.T.; Barois, P. *Europhys. Lett*. **2003**, *63*, 840–845.
(45) Toner, J. *Phys. Rev. B* **1991**, 43, 8289–8296.
(46) Petit, M.; Barois, P.; Nguyen, H.T. *Europhys. Lett*. **1996**, *36*, 185–190.
(47) Barois, P.; Nobili, M.; Petit, M. *Mol. Cryst. Liq. Cryst.* **1997**, *302*, 215–221.
(48) Petit, M.; Nobili, M.; Barois, P. *Eur. Phys. J.* **1998**, *B6*, 341–345.
(49) Isaert, N.; Navailles, L.; Barois, P.; Nguyen, H.T. *J. Phys. II France* **1994**, *4*, 1501–1518.
(50) Aubry, S. *Solitons and Condensed Matter Physics*, Bishop, A.R. and Schneider, T., Eds.; Springer: Berlin, 1978; pp 264–278.
(51) Galerne, Y. *Phys. Rev. Lett.* 1994, 72, 1299 and reply L. Navailles, Barois, P.; and Nguyen H.T. Phys. Rev. Lett. **1994,** *72*, 1300–1300
(52) Barois, M.; Heidelbach, F.; Navailles, L.; Nguyen, H.T.; Nobili, M.; Petit, M.; Pindak, R.; Riekel, C. *Eur. Phys. J.* **1999**, *B11*, 455–462.
(53) Gido, S.P.; Gunther, J.; Thomas, E.L.; Hoffman, D. *Macromolecules*, **1993**, *26*, 4506–4520.
(54) Gido, S.P.; Thomas, E.L. *Macromolecules* **1994**, *27*, 849–861.
(55) Gido, S.P.; Thomas, E.L. *Macromolecules* **1997**, *30*, 3739–3746.
(56) He, S.-J.; Lee, C.; Gido, S.P.; Yu, S.M.; Tirrell, D.A. *Macromolecules* **1998**, *31*, 9387–9389.
(57) Lubensky, T.C.; Kamien, R.D.; Stark, H. *Mol. Cryst. Liq. Cryst*. **1996**, *288*, 15–23.
(58) Kamien, R.D.; Lubensky, T.C. *J. Phys. II* **1997**, *7*, 157–163.
(59) Larche, F.; Appell, J.; Porte, G.; Bassereau, P.; Marignan, J. *Phys. Rev. Lett*. **1985**, *56*, 1700–1703.
(60) Safinya, C.; Roux, D.; Smith, G.S.; Sinha, S.K.; Dimon, P.; Clark, N.; Bellocq, A.M. *Phys. Rev. Lett.* **1986**, *57*, 2718–2721.
(61) Helfrich, W. *J. Phys. France* **1978**, *39*, l199–1208.
(62) Nelson, D.R.; Toner, J. *Phys. Rev*. **1981**, *B24*, 363–387.
(63) Moreau, P.; Navailles, L.; Giermanska-Kahn, J.; Mondain-Monval, O.; Nallet, F.; Roux, D. *Europhys. Lett.* **2006**, *73*, 49–54.
(64) Kleman, M. *Points, Lines and Walls*; J. Wiley and Sons: New York, 1983.